Theoretical investigation of confocal microscopy using an elliptically polarized cylindrical vector laser beam: Visualization of quantum emitters near interfaces

Stepan Boichenko*

Irkutsk Branch of the Institute of Laser Physics of the Russian Academy of Sciences, Lermontov Street 130a, 664033 Irkutsk, Russian Federation

(Received 29 December 2017; published 12 April 2018)

We theoretically study laser-scanning confocal fluorescence microscopy using elliptically polarized cylindrical vector excitation light as a tool for visualization of arbitrarily oriented single quantum dipole emitters located (1) near planar surfaces enhancing fluorescence, (2) in a thin supported polymer film, (3) in a freestanding polymer film, and (4) in a dielectric planar microcavity. It is shown analytically that by using a tightly focused azimuthally polarized beam, it is possible to exclude completely the orientational dependence of the image intensity maximum of a quantum emitter that absorbs light as a pair of incoherent independent linear dipoles. For linear dipole quantum emitters, the orientational independence degree higher than 0.9 can normally be achieved (this quantity equal to 1 corresponds to completely excluded orientational dependence) if the collection efficiency of the microscope objective and the emitter's total quantum yield are not strongly orientationally dependent. Thus, the visualization of arbitrarily oriented single quantum emitters by means of the studied technique can be performed quite efficiently.

DOI: 10.1103/PhysRevA.97.043825

I. INTRODUCTION

Fluorescent visualization of single quantum emitters (SQEs)—such as single dye molecules, single quantum dots, single color centers—is an essential part of modern single-molecule fluorescence microscopy techniques, which are widely used today and provide a powerful toolkit for many research areas [1,2]. In particular, single-molecule localization microscopy techniques are exploited to perform super-resolution imaging in live cell studies and other medical and biological applications [3–6]. Excited-state tautomerization has been observed by means of laser-scanning confocal fluorescence microscopy [7], monitoring of the polymer dynamics by means of far-field fluorescence spectromicroscopy has been demonstrated [8], and mechanistic studies of chemical reactions at the single-molecule level can be performed by means of single-molecule fluorescence microscopy [9]. Single-molecule fluorescence microscopy has many other applications in chemistry and materials science [1]. Another scientific area that exploits single-molecule fluorescence microscopy is the development of single-molecule-based single-photon sources [10–16] for quantum informatics and quantum cryptography.

The orientations of the transition dipole moments (TDMs) of SQEs and the polarization of the excitation laser light field play an important role in single-molecule studies [17,18] as the excitation probability of a single molecule significantly depends on the mutual orientation of the molecule's TDM and the laser light field vector. This property of the excitation probability makes the visualization of arbitrarily oriented SQEs a challenging problem for single-molecule fluorescence microscopy. For some applications it is not necessary to observe SQEs of different orientations, but some other applications do require visualization of all SQEs regardless of their orientations in the sample area under investigation. For example, single-molecule counting is an important tool in biological researches [19–21], but without the opportunity to visualize all SQEs in a tissue under investigation one can lose some information, causing an incomplete analysis. Slow rotational dynamics of single fluorescent molecules can be observed by means of single-molecule polarization microscopy and was exploited in biological studies [22], but to perform such observations effectively, one needs to visualize arbitrarily oriented SQEs. The visualization of arbitrarily oriented SQEs is an important task for chemistry and materials science as well [7,8,23,24]. For example, in chemical investigations, tautomerism processes can be observed by means of single-molecule fluorescence microscopy at the single-molecule level [7,25,26]. Here, a single molecule under investigation transforms from one tautomeric form to another during the experiment. As the molecule in different tautomeric forms has different orientations, the visualization of arbitrarily oriented single molecules turns out to be indispensable in this case. Single-molecule spectromicroscopy can be used as a tool for multicolor materials nanodiagnostics in materials science [8,23]. In this case, the visualization of all fluorescent molecules is desirable as well. The development of single-molecule-based single-photon sources [10,12,14–16] is another application where the visualization of arbitrarily oriented SQEs is required. So, the tasks appearing in these applications give rise to a search for solutions to the problem of visualization of arbitrarily oriented SQEs.

The first attempt to observe SQEs of different orientations was made by Betzig and Chichester in 1993 [27]. They studied carbocyanine dye molecules in polymethylmethacrylate film by means of near-field scanning optical microscopy and have demonstrated the visualization of molecules with TDMs both

*ste89@yandex.ru

parallel and perpendicular to the sample plane in the same experiment. Later, the visualization of single molecules with different TDM orientations was demonstrated by means of defocused wide-field microscopy [28] and laser-scanning confocal fluorescence microscopy (LSCFM) [29]. During the last two decades, many single-molecule orientational microscopy techniques have been developed and today orientational imaging of SQEs is an independent branch of single-molecule spectromicroscopy. However, many of them are adapted for the visualization of SQEs of different but not all possible orientations; normally, the researchers aim to observe single molecules with TDM parallel and perpendicular to a sample plane simultaneously, but molecules with TDMs of intermediate orientations can remain invisible. To the best of our knowledge, only two single-molecule microscopy techniques are able to perform the visualization of all SQEs regardless of their TDM orientations in the same experiment: LSCFM using an excitation light beam with a spatially inhomogeneous polarization [29–36] and near-field scanning optical microscopy using a tip of special shape [37]. Both of these techniques exploit the combination of the scanning process and the spatial variation of the focal-region excitation laser light field polarization: in fact, an image of a single molecule under investigation maps the distribution of the light field in the focal region. In different points of the focal region the polarization takes on different values, taking on all its possible values in the entire focal region; it provides an opportunity to visualize SQEs of all orientations.

The starting point of the orientational LSCFM is [29] where Sick, Hecht, and Novotny suggested using an annular linearly polarized excitation beam. They have demonstrated that this method allows one to visualize x-, y-, and z-oriented SQEs in the same experiment (x, y, and z are Cartesian coordinates). On the one hand the suggested technique solved the problem of the visualization of arbitrarily oriented SQEs, but on the other hand the images of y-oriented molecules were 10 times dimmer than images of x-oriented molecules and it worked only for molecules near air–polymer interfaces. So, an improvement of the technique was desirable. In [31] a robust amplitude-phase mask for the excitation beam was suggested and the difference between the brightest and the dimmest molecule was significantly reduced (it amounted to about 2 times instead of 10), but that mask was too complicated and it led to significant losses of the excitation beam energy. A radially polarized excitation beam as a tool for visualization of arbitrarily oriented SQEs was suggested in [30] for the first time. Depending on the beam intensity profile and microscope objective aperture, the image intensity difference between the dimmest and the brightest molecules can be strongly reduced, which attracted significant interest in LSCFM using this beam [7,31,32,34,38,39]. Later, a generalized cylindrical vector beam was suggested [35] and further improvement of the technique was demonstrated. Subsequently, an elliptically polarized cylindrical vector beam (EPCVB) was explored and nearly complete elimination of the single-molecule image intensity has been reached [36]. In the present study, we continue developing the LSCFM technique using EPCVB (LSCFM-EPCVB technique) for the visualization of arbitrarily oriented SQEs.

More specifically, we adapt the LSCFM-EPCVB technique for visualization of arbitrarily oriented SQEs located near different planar interfaces. Previously, we have demonstrated the possibility of highly efficient visualization of arbitrarily oriented SQEs located in a homogeneous medium (like a thick polymer film or a bulk crystal) [36] and inside a 99%-collection-efficiency optical antenna [40]. However, there exist many single-molecule applications, in which other different single-molecule-doped planar structures are studied. First, single-dye-molecule-doped thin polymer films supported by a cover glass were the objects of many investigations [1,8] and in some cases the visualization of single molecules of different orientations is desirable [23,41–45]. Second, surface-enhanced fluorescence is widely used today [46] and for some of its applications single-molecule orientational imaging plays an important role [47–50]. Next, the visualization of SQEs near metallo-dielectric structures for surface-plasmon-coupled fluorescence [51–62], in planar optical microcavities [14,38,63–68], and in freestanding polymer films [69–72] is widely used. So, the aim of our present work is to explore the applicability of the LSCFM-EPCVB technique for visualization of arbitrarily oriented SQEs located in the above-mentioned media via simulations, and to analyze the focusing properties of the EPCVB.

The paper is organized as follows. In Sec. II we express the theory exploited for the simulation of LSCFM images of SQEs and explain the antenna properties of SQEs. Further, we describe the approaches that are applied to quantify the efficiency of the visualization of arbitrarily oriented SQEs, express the focusing equations for EPCVBs, and consider the interaction of tightly focused EPCVBs with SQEs. In Sec. III we analyze the interaction of a focused EPCVB with a SQE extensively. Finally, in Sec. IV we study numerically the visualization of arbitrarily oriented SQEs located (1) on surfaces that enhance SQEs' fluorescence, (2) in a polymer film on a glass substrate, (3) in a freestanding polymer film, and (4) in a dielectric microcavity.

II. THEORY

Figure 1 shows the sketch of a laser-scanning confocal fluorescence microscope setup. The polarization state of the collimated linearly polarized laser beam is modified by a polarization converter and then the beam is focused by a microscope objective to excite the fluorescence of SQEs. The fluorescence emitted by a SQE is collected by the same objective. The sample is moved with a three-dimensional (3D) scanner to obtain scanning fluorescent images of SQEs. Note that normally two-dimensional images are recorded (scanning is performed in the plane normal to the objective optical axis) and the objective can be shifted along the optical axis to set an optimal longitudinal position of the geometrical focus. The space between the objective and the sample can be filled with immersion fluid to exclude the influence of the lower surface of the sample.

A. Simulation of LSCFM images of single quantum emitters

We consider SQEs of two types: a linearly polarized electric dipole oscillator (linear dipole) and a pair of two incoherent

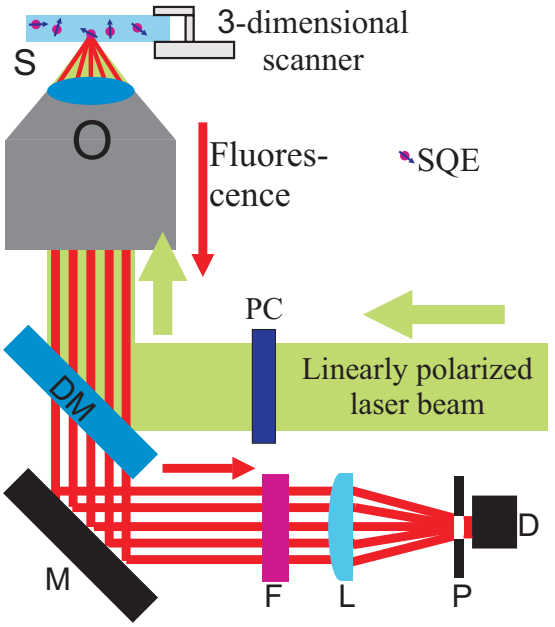

FIG. 1. The sketch of a LSCF microscope system. A collimated linearly polarized laser beam is directed onto a polarization converter (PC), then it is reflected by a dichroic mirror (DM) and focused by a microscope objective (O) onto a sample (S). The sample is assumed to be a transparent solid matrix doped with single quantum fluorescent emitters (SQEs). The emitters are excited by a focused laser beam and the emitted fluorescence is collected by the objective. The collected emission is passed through the dichroic mirror, directed by a mirror (M) onto a filter (F) to reject residual laser excitation light, then it is focused by a lens (L) onto a detector (D) through a pinhole (P).

mutually orthogonal linear electric dipoles [two-dimensional (2D) dipole]. The majority of organic dye molecules, color centers in bulk crystals, and many other SQEs emit and absorb light as linear dipoles; some other SQEs, as 2D dipoles: for example, nitrogen-vacancy centers in diamond [39,73,74]. The LSCFM image intensity distribution of a SQE can be calculated as

$$I(\mathbf{r},\mathbf{d}_a,\mathbf{d}_e) = \eta_{\text{det}} T_{\text{opt}} \eta_{\text{coll}}(\mathbf{d}_e) R(\mathbf{r},\mathbf{d}_a,\mathbf{d}_e), \tag{1}$$

where η_{det} is the quantum efficiency of the LSCFM system detector, T_{opt} the total transmittance of the microscope optics, η_{coll} the collection efficiency of the microscope objective, $R(\mathbf{r},\mathbf{d}_a,\mathbf{d}_e)$ the fluorescence emission rate of the SQE; $\mathbf{r}$ is a radius vector of a focal-region point, and $\mathbf{d}_a$ and $\mathbf{d}_e$ are unit vectors directed along absorption and emission transition dipole moments (TDMs) of the SQE, respectively. For many chromophores and other emitters, the absorption and the emission TDMs are collinear vectors, but there are some exceptions to this rule [75]. Moreover, recently it has been demonstrated that the angle between the absorption and the emission TDMs of a single molecule can be significantly large [76]. So, in general the absorption and the emission TDMs are not collinear vectors and we keep them as different vectors in the equations. However, we will assume in our calculations that these vectors are collinear unless otherwise specified. η_{det} and T_{opt} are supposed to be independent of a SQE's orientation, which makes them constants in Eq. (1). As the focal distance of the objective is significantly larger in magnitude than the focal region (several millimeters vs hundreds of nanometers), η_{coll} is supposed to be independent of the focal coordinates. The fluorescence emission rate of a three-level quantum system irradiated with a continuous-wave (cw) excitation can be calculated as [75]

$$R_{cw}(\mathbf{r},\mathbf{d}_a,\mathbf{d}_e) = \frac{Q(\mathbf{d}_e)\Gamma_{ex}(\mathbf{r},\mathbf{d}_a)}{1+\frac{\Gamma_{TS}+\gamma_{ST}}{\gamma_{ST}}\frac{\Gamma_{ex}(\mathbf{r},\mathbf{d}_a)}{\gamma_f(\mathbf{d}_e)+\Gamma_{TS}}}. \tag{2}$$

Here $Q(\mathbf{d}_e)$ is the total quantum yield of the system, $\Gamma_{ex}(\mathbf{r},\mathbf{d}_a)$ the excitation rate, Γ_{TS} the intersystem crossing rate, γ_{ST} the phosphorescence decay rate, $\gamma_f(\mathbf{d}_e)$ the total fluorescence decay rate. For normal excitation modes the condition $\Gamma_{ex}(\mathbf{r},\mathbf{d}_a) \ll \gamma_f(\mathbf{d}_e)$ is valid and for the majority of quantum systems Γ_{TS} and γ_{ST} are comparable in magnitude, which makes the second term in the denominator of Eq. (2) small in magnitude. For this reason, we will consider excitation modes, for which the fluorescence emission rate can be approximated as

$$R_{cw}(\mathbf{r},\mathbf{d}_a,\mathbf{d}_e) = Q(\mathbf{d}_e)\Gamma_{ex}(\mathbf{r},\mathbf{d}_a). \tag{3}$$

For normal pulsed excitation modes, the condition $\tau_p \ll \tau_f \ll 1/\nu$ is satisfied. Here τ_p is the pulse duration time, τ_f is the fluorescence lifetime, and ν is the pulse repetition rate. Under this condition, the probability to excite a SQE by a single excitation pulse can be approximated as $P_{ex}(\mathbf{r},\mathbf{d}_a) = \tau_p\Gamma_{ex}(\mathbf{r},\mathbf{d}_a)$ and the fluorescence emission rate as

$$R_p(\mathbf{r},\mathbf{d}_a,\mathbf{d}_e) = \nu\tau_p Q(\mathbf{d}_e)\Gamma_{ex}(\mathbf{r},\mathbf{d}_a). \tag{4}$$

Here, the relationship $R_p = \nu Q(\mathbf{d}_e)P_{ex}$ has been applied. Generalizing Eqs. (4) and (3), we conclude

$$R(\mathbf{r},\mathbf{d}_a,\mathbf{d}_e) = C\,Q(\mathbf{d}_e)\Gamma_{ex}(\mathbf{r},\mathbf{d}_a), \tag{5}$$

where $C = \nu\tau_p$ for pulsed excitation and $C = 1$ for cw excitation is a constant. Substituting Eq. (5) into Eq. (1), we derive

$$I(\mathbf{r},\mathbf{d}_a,\mathbf{d}_e) = A\eta_{\text{coll}}(\mathbf{d}_e)Q(\mathbf{d}_e)\Gamma_{ex}(\mathbf{r},\mathbf{d}_a), \tag{6}$$

where A is a constant defined as $A = \nu\tau_p\eta_{\text{det}}T_{\text{opt}}$ for pulsed excitation and $A = \eta_{\text{det}}T_{\text{opt}}$ for cw excitation.

The microscope objective fluorescence collection efficiency in Eq. (6) reads as

$$\eta_{\text{coll}}(\mathbf{d}_e) = \frac{\gamma_{\text{coll}}(\mathbf{d}_e)}{\gamma_r(\mathbf{d}_e)}, \tag{7}$$

where $\gamma_{\text{coll}}(\mathbf{d}_e)$ is the radiative fluorescence rate collected by the objective and $\gamma_r(\mathbf{d}_e)$ is the total radiative fluorescence decay rate. The quantum yield of a SQE is defined as

$$Q(\mathbf{d}_e) = \frac{\gamma_r(\mathbf{d}_e)}{\gamma_r(\mathbf{d}_e)+\gamma_{\text{loss}}(\mathbf{d}_e)+\gamma_{nr}}, \tag{8}$$

where $\gamma_{\text{loss}}(\mathbf{d}_e)$ is the rate of near-field energy fluorescence dissipation and γ_{nr} is the intrinsic nonradiative decay rate. The denominator in Eq. (8) represents the total fluorescence decay rate $\gamma_f(\mathbf{d}_e)$.

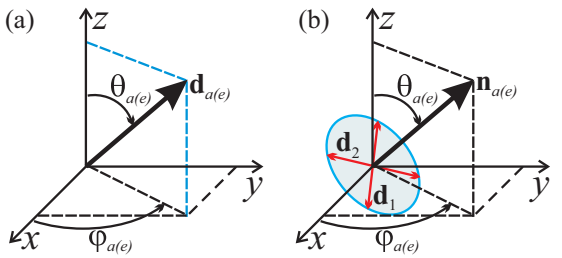

FIG. 2. Geometrical models of (a) the linear dipole SQE and (b) the 2D dipole SQE.

1. Optical model of the linear dipole emitter and of the 2D dipole emitter

Figure 2 shows the geometrical models of (a) the linear dipole emitter and of (b) the 2D dipole emitter. A linear dipole emitter is represented by a dipole vector oscillating along the direction assigned by the angles $\theta_{a(e)}$ and $\varphi_{a(e)}$ in a spherical coordinate system. The indices a and e are associated with absorption and emission, respectively. In the 2D dipole model, it is supposed that the transition dipole moment of a SQE is twofold degenerate and the emitter emits and absorbs light as any pair of mutually orthogonal independent and incoherent linear dipoles lying in the plane which the vector $\mathbf{n}_{a(e)}$ is normal to. This vector is defined by the angles $\theta_{a(e)}$ and $\varphi_{a(e)}$ in spherical coordinates and the plane where the dipoles lie is called the bright plane [75].

The excitation rate of linear dipole SQE fluorescence is given by [75]

$$\Gamma_{ex}^{ld}(\mathbf{r},\mathbf{d}_a) = k|\mathbf{E}(\mathbf{r})\cdot\mathbf{d}_a|^2, \tag{9}$$

where $\mathbf{E}(\mathbf{r})$ is the laser excitation light field vector and k is a constant defined by chemical properties of the emitter and the host matrix, and it does not depend on the absorption TDM orientation. For a 2D dipole SQE, the excitation rate reads as [77]

$$\Gamma_{ex}^{2D}(\mathbf{r},\mathbf{n}_a) = k\left[\left|\mathbf{E}(\mathbf{r})\cdot\mathbf{d}_1^{(a)}\right|^2 + \left|\mathbf{E}(\mathbf{r})\cdot\mathbf{d}_2^{(a)}\right|^2\right]. \tag{10}$$

To find the decay rates exploited in Eqs. (8) and (7) for a 2D dipole SQE, we need to calculate the respective rates of the two in-bright-plane linear dipole SQEs separately and then calculate 2D dipole rates as averages of the two linear dipoles' SQE rates [75].

2. General description of a layered structure

Figure 3 shows the structure of a layered medium that is considered here. We assume that a layered medium is supported by a substrate with refractive index n_{sub}, the microscope objective is located under the substrate, and the refractive index of the substrate coincides with the index of the objective. The layered medium consists of two planar mirrors and a layer doped with SQEs between the mirrors. Each layer i is described by its refractive index n_i and its thickness d_i.

The upper mirror consists of N layers and the lower mirror of M layers. The space over the film is supposed to be infinite and characterized by the refractive index n_{out}. In general, any layer of this structure can be either dielectric or metallic. Knowing all refractive indices and thicknesses, one can calculate all

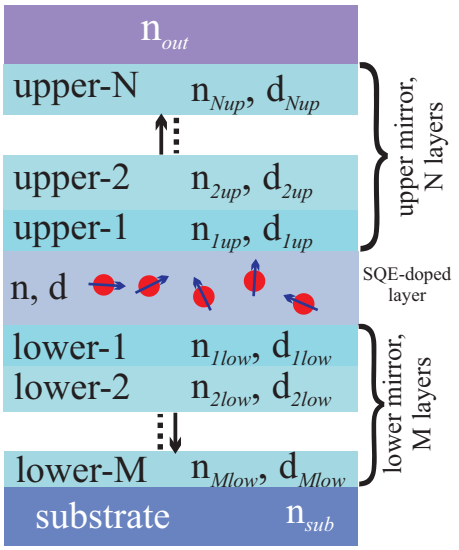

FIG. 3. The generalized structure of a layered medium under consideration.

reflection and transmission coefficients of the mirrors. To calculate these coefficients, we exploit the transfer matrix method [78]. Finally, a layered medium is described by the following four vectors (see Fig. 3): the thickness vector of the lower mirror $\mathbf{d}_l = (d_{1l}, d_{2l}, \ldots, d_{Ml})$, the refractive index vector of the lower mirror $\mathbf{n}_l = (n_{1l}, n_{2l}, \ldots, n_{Ml})$, the thickness vector of the upper mirror $\mathbf{d}_{up} = (d_{1up}, d_{2up}, \ldots, d_{Nup})$, the refractive index vector of the upper mirror $\mathbf{n}_{up} = (n_{1up}, n_{2up}, \ldots, n_{Nup})$. To adapt the model for a structure with only an upper or a lower mirror, we state the vectors describing the absent mirror to be $\mathbf{d}_i = (0,0,\ldots,0)$ and $\mathbf{n}_i = (n,n,\ldots,n)$, where $i = l$ or $i = up$.

The generalized sketch of a layered medium for calculation of the light field inside it is expressed in Fig. 4. The origin of the coordinate system coincides with the position of the SQE under observation. The coordinates z_1 and z_2 are the longitudinal positions of the lower and upper boundaries of the SQE-doped layer, respectively. The reflection and transmission coefficients are expressed in the figure. The indices in and out denote whether the light field starts propagation inside the film or outside of it, respectively. The indices l and up distinguish the lower and the upper mirror, respectively, as before. The indices s and p denote s and p polarization, respectively. Calculating these coefficients by means of the transfer matrix method, we

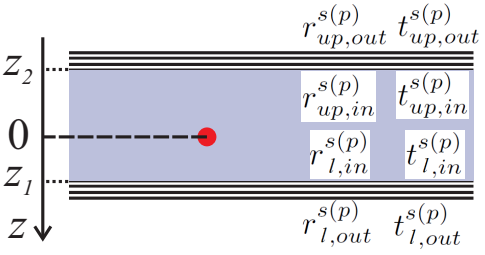

FIG. 4. The longitudinal position of a SQE in the layered medium. Optical properties of a layered medium are described by the transmission and reflection coefficients.

are able to analyze the emitter's fluorescence and the focal-region excitation light field.

3. Calculation of a SQE fluorescence in a layered medium

To calculate the emission rates of a SQE inside a layered medium, we exploit the angular spectrum representation of the emission light field of a linear dipole emitter [75]. The fluorescence radiative decay rate of a SQE and the emission power collected by the objective are calculated from the far-field emission pattern of the emitter. Taking into account multiple reflections inside the layered structure and knowing reflection and transmission coefficients expressed in Fig. 4, the normalized far-field emission pattern of a linear dipole emitter was derived:

$$\begin{aligned} J_{ld}^{l(up)}(\theta,\varphi;\theta_e,\varphi_e) = \frac{3n_{l(up)}}{8\pi n}\Big\{&\left|\Psi_{l(up)}^{(1)}(\theta)\right|^2\cos^2\theta\sin^2\theta_e \\ &\times\cos^2(\varphi_e-\varphi)+\left|\Psi_{l(up)}^{(2)}(\theta)\right|^2\cos^2\theta_e\sin^2\theta \\ &-0.5\,\mathrm{Re}\left[\Psi_{l(up)}^{(1)}(\theta)\Psi_{l(up)}^{*(2)}(\theta)\right]\sin 2\theta\sin 2\theta_e\cos(\varphi_e-\varphi) \\ &+\left|\Psi_{l(up)}^{(3)}(\theta)\right|^2\sin^2\theta_e\sin^2(\varphi_e-\varphi)\Big\}. \end{aligned} \tag{11}$$

Here, $J(\theta,\varphi;\theta_e,\varphi_e)$ is the far-field emission power of the SQE in the direction $\mathbf{n}=(\sin\theta\cos\varphi,\sin\theta\sin\varphi,\cos\theta)$, normalized to the fluorescence radiative decay rate of this SQE in the medium with the refractive index n, not bounded with the mirrors. Angles θ_e and φ_e assign the emission TDM unit vector as shown in Fig. 2; θ and φ are the far-field angles of a spherical coordinate system. The functions Ψ in Eq. (11) are given by

$$\begin{aligned} \Psi_{l(up)}^{(1)}(\theta) &= \frac{n_{l(up)}}{n}F_{l(up)}^{p}(\theta)\left\{1-r_{up(l),in}^{p}(\theta)\right. \\ &\quad\left.\times\exp\left[2ik_z^{l(up)}(\theta)|z_{up(l)}|\right]\right\}, \end{aligned} \tag{12a}$$

$$\begin{aligned} \Psi_{l(up)}^{(2)}(\theta) &= \frac{n_{l(up)}}{n}G_{l(up)}(\theta)F_{l(up)}^{p}(\theta)\left\{1+r_{up(l),in}^{p}(\theta)\right. \\ &\quad\left.\times\exp\left[2ik_z^{(l(up))}(\theta)|z_{up(l)}|\right]\right\}, \end{aligned} \tag{12b}$$

$$\begin{aligned} \Psi_{l(up)}^{(3)}(\theta) &= G_{l(up)}(\theta)F_{l(up)}^{p}(\theta)\left\{1+r_{up(l),in}^{s}(\theta)\right. \\ &\quad\left.\times\exp\left[2ik_z^{(l(up))}(\theta)|z_{up(l)}|\right]\right\}, \end{aligned} \tag{12c}$$

where the functions G and F are given by

$$G_{l(up)}(\theta)=\frac{\cos\theta}{\sqrt{(n/n_{l(up)})^2-\sin^2\theta}}, \tag{13}$$

$$F_{l(up)}^{s(p)}(\theta)=\frac{t_{l(up),in}^{s(p)}(\theta)\exp\left[ik_z^{l(up)}(\theta)|z_{l(up)}|\right]}{1-r_{l,in}^{s(p)}(\theta)r_{up,in}^{s(p)}(\theta)\exp\left[2ik_z^{(n)}(\theta)(z_l-z_{up})\right]}, \tag{14}$$

and the longitudinal component of the wave vector inside the SQE-doped medium reads as

$$k_z^{l(up)}(\theta)=k_0\sqrt{n^2-n_{l(up)}^2\sin^2\theta}, \tag{15}$$

where k_0 is the vacuum wave number of the emitted light. The emission pattern for a 2D dipole SQE is calculated as

$$\begin{aligned} J_{2D}^{l(up)}(\theta,\varphi;\theta_e,\varphi_e) = \frac{3n_{l(up)}}{16\pi n}\Big\{&\left|\Psi_{l(up)}^{(1)}(\theta)\right|^2[\cos^2\theta_e \\ &\times\cos^2(\varphi-\varphi_e)+\sin^2(\varphi-\varphi_e)]\cos^2\theta+\left|\Psi_{l(up)}^{(2)}(\theta)\right|^2 \\ &\times\sin^2\theta_e\sin^2\theta+0.5\,\mathrm{Re}\left[\Psi_{l(up)}^{(1)}(\theta)\Psi_{l(up)}^{*(2)}(\theta)\right]\sin 2\theta \\ &\times\sin 2\theta_e\cos(\varphi_e-\varphi)+\left|\Psi_{l(up)}^{(3)}(\theta)\right|^2[\cos^2\theta_e\sin^2(\varphi_e-\varphi) \\ &+\cos^2(\varphi_e-\varphi)]\Big\}. \end{aligned} \tag{16}$$

The normalized radiative fluorescence rate collected by the microscope objective and the normalized total radiative decay rate of a linear dipole SQE and of a 2D dipole emitter are given by

$$\frac{\gamma_{\mathrm{coll}}^{ld(2D)}(\theta_e)}{\gamma_{\mathrm{rad}}^{0}}=\int_0^{\theta_m}\sin\theta d\theta\int_0^{2\pi}J_{ld(2D)}^{l}(\theta,\varphi,\theta_e,\varphi_e)d\varphi, \tag{17}$$

$$\frac{\gamma_{\mathrm{rad}}^{ld(2D)}(\theta_e)}{\gamma_{\mathrm{rad}}^{0}}=\int_0^{\pi}\sin\theta d\theta\int_0^{2\pi}J_{ld(2D)}(\theta,\varphi,\theta_e,\varphi_e)d\varphi, \tag{18}$$

where

$$J_{ld(2D)}(\theta,\varphi,\theta_e,\varphi_e)=\begin{cases}J_{ld(2D)}^{l}(\theta,\varphi,\theta_e,\varphi_e), & 0\leqslant\theta\leqslant\frac{\pi}{2},\\ J_{ld(2D)}^{up}(\theta,\varphi,\theta_e,\varphi_e), & \frac{\pi}{2}<\theta\leqslant\pi;\end{cases} \tag{19}$$

$\gamma_{\mathrm{rad}}^{0}$ is the radiative fluorescence decay rate of a SQE in the medium with the refractive index n, and θ_m is the angular aperture of the microscope objective.

The expressions for calculating the normalized fluorescence decay rates have been derived via the evaluation of the interaction of a SQE under consideration with the light field emitted by the SQE and turned back to the emitter by the layered medium; this approach is described in detail in [75]. For a linear dipole parallel to the layers of a layered structure we obtained

$$\begin{aligned} \frac{\gamma_{\mathrm{rad}}^{pl}+\gamma_{\mathrm{loss}}^{pl}}{\gamma_{\mathrm{rad}}^{0}} = 1+\int_0^{\infty}u\,\mathrm{Re}\left\{\frac{f_1^s+f_2^s+2f_1^sf_2^s}{u_z\left(1-f_1^sf_2^s\right)}\right. \\ \left.-u_z\frac{f_1^p+f_2^p-2f_1^pf_2^p}{1-f_1^pf_2^p}\right\}du \end{aligned} \tag{20}$$

and for a dipole perpendicular to the planes

$$\frac{\gamma_{\mathrm{rad}}^{z}+\gamma_{\mathrm{loss}}^{z}}{\gamma_{\mathrm{rad}}^{0}}=1+\int_0^{\infty}u^3\,\mathrm{Re}\left[\frac{f_1^p+f_2^p+2f_1^pf_2^p}{u_z\left(1-f_1^pf_2^p\right)}\right]du. \tag{21}$$

Here the following functions have been used:

$$f_1^{s(p)}(u)=r_{up,in}^{s(p)}(u)\exp[-2ik_0nu_z(u)z_{up}], \tag{22a}$$

$$f_2^{s(p)}(u)=r_{l,in}^{s(p)}(u)\exp[-2ik_0nu_z(u)z_l], \tag{22b}$$

where $u=k_\rho/k$ and $u_z(u)=k_z/k=\sqrt{1-u^2}$; k is the wave number of the emitted light, and k_ρ and k_z are the plane and the longitudinal components of the wave vector, respectively.

Finally, for an arbitrarily oriented linear dipole SQE we have

$$\frac{\gamma_{\rm rad}(\mathbf{d}_e)+\gamma_{\rm loss}(\mathbf{d}_e)}{\gamma^0_{\rm rad}} = \left(\frac{\gamma^z_{\rm rad}+\gamma^z_{\rm loss}}{\gamma^0_{\rm rad}}\right)\cos^2\theta_e + \left(\frac{\gamma^{pl}_{\rm rad}+\gamma^{pl}_{\rm loss}}{\gamma^0_{\rm rad}}\right)\sin^2\theta_e \quad (23)$$

and for an arbitrarily oriented 2D dipole SQE

$$\frac{\gamma_{\rm rad}(\mathbf{n}_e)+\gamma_{\rm loss}(\mathbf{n}_e)}{\gamma^0_{\rm rad}} = \left(\frac{\gamma^z_{\rm rad}+\gamma^z_{\rm loss}}{\gamma^0_{\rm rad}}\right)\sin^2\theta_e + \left(\frac{\gamma^{pl}_{\rm rad}+\gamma^{pl}_{\rm loss}}{\gamma^0_{\rm rad}}\right)\frac{\cos^2\theta_e+1}{2}. \quad (24)$$

4. Calculation of tightly focused excitation laser light field in layered structures

To calculate a tightly focused light field in a layered medium, we exploit Richards-Wolf theory [79]. The model was reviewed recently and is described in detail in [75]; Meixner's group adapted it for planar microcavities [80] to take into account the multiple reflections inside a cavity followed by the interference of the reflected light fields. A layered medium that we consider in the present paper is a planar-cavity-like structure and the focusing equations derived in [80] can be readily adapted for our simulations. So, they were adapted and are exploited hereunder. We suppose the microscope objective to obey the Abbe sine condition.

B. Quantification of the efficiency of arbitrarily oriented SQE visualization techniques

1. Comparing the dimmest and the brightest orientations

To quantify the ability of a single-molecule microscopy technique to visualize arbitrarily oriented SQEs, we exploit the approach of comparing the dimmest and the brightest orientations that has been proposed previously [36,40]. Hereunder, we will describe it in detail. The image intensity distribution of a SQE with the unit absorption TDM $\mathbf{d}_a = (\sin\theta_a\cos\varphi_a, \sin\theta_a\sin\varphi_a, \cos\theta_a)$ and the unit emission TDM $\mathbf{d}_e = (\sin\theta_e\cos\varphi_e, \sin\theta_e\sin\varphi_e, \cos\theta_e)$ can be calculated according to Eq. (6) and depends on the orientations of the emitter's dipoles. Hence, the intensity maximum of an image depends on the orientations too. Trying all possible orientations (mathematically it means variation of angles $\theta_{a(e)}$ from 0 to π and $\varphi_{a(e)}$ from 0 to 2π), we can analyze images of SQEs of all orientations. Knowing the image intensity distributions of SQEs of all possible orientations, we are able to find the intensity maxima of each image. Then we find the smallest maximum among these maximums $\max(I_{\rm dim})$ (the image of a SQE of the dimmest orientation) and the biggest maximum $\max(I_{br})$ (the image of a SQE of the brightest orientation). The parameter

$$\varepsilon_{im} = \frac{\max(I_{\rm dim})}{\max(I_{br})} \quad (25)$$

serves as a measure of the efficiency of visualization of arbitrarily oriented SQEs. It quantifies the degree of independence of SQEs' image intensity maximums on the SQEs' orientations, briefly, the orientational independence degree (OID). This parameter can take on values between 0 and 1; $\varepsilon = 0$ indicates that emitters of some orientations are invisible and $\varepsilon = 1$ states that the visualization of SQEs of all orientations is equally successful. So, to have maximally efficient visualization of arbitrarily oriented SQEs, one should reach as high a value of ε as possible.

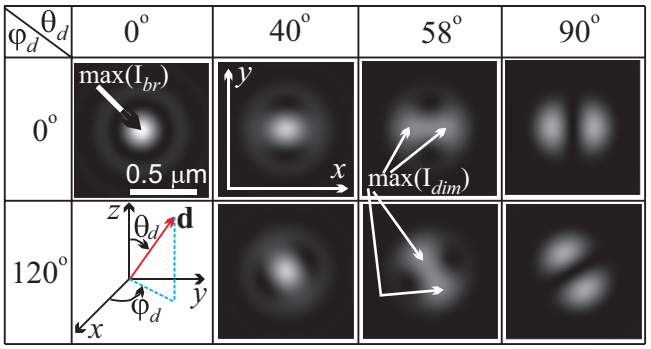

FIG. 5. The explanation to the approach of comparing the dimmest and the brightest orientations.

To explain the approach of comparing the dimmest and the brightest orientations, we will demonstrate an example by applying it to LSCFM using a radially polarized excitation laser beam as a tool for visualization of arbitrarily oriented linear dipole SQEs in a homogeneous medium (Fig. 5). The TDMs $\mathbf{d}_a$ and $\mathbf{d}_e$ are assumed to be collinear vectors and the polar and azimuthal angles are denoted θ_d and φ_d, respectively. First, the set of images of SQEs of all possible orientations was calculated: the angle θ_d was varied from 0 to 90° with the step of 1° and the angle φ from 0 to 360° with the step of 1°. Figure 5 displays images of SQEs of some orientations. The analysis of all calculated images showed that the emitters with $\theta_d = 58°$ (regardless of φ_d) were the dimmest and the images of z-oriented emitters were the brightest. The degree of intensity maximum orientational independence (25) amounts to 0.45.

2. Comparing the most excitable and the least excitable orientations

According to Eq. (6), the image intensity of a SQE is a product of the emitter's collection function [the multiplier $\eta(\mathbf{d}_e)Q(\mathbf{d}_e)$] and the emitter's excitation efficiency (the multiplier $|\mathbf{E}(\mathbf{r})\cdot\mathbf{d}_a|^2$). In some layered structures the emission-power difference between emitters of different orientations may be orders of magnitude. This occurs, for example, for dye molecules near a metal film [81]. Applying the approach of comparing the dimmest and the brightest orientations, we aim to compensate for the difference in the collection functions of SQEs of different orientations by creating a contrary orientational difference in excitation probability of the emitters. However, in some investigations the elimination of the excitation rate orientational dependence is of higher importance than the elimination of the image intensity maximum orientational dependence as the behavior of SQEs normally depends on the strength of the interaction between a SQE and the excitation light field. On the other hand, if the orientational dependence of the collection function is as big as several orders of magnitude, the creation of a similarly big difference in the excitation field components will be required, which hardly can

be performed in a controllable way. Taking this into account, we develop an additional way of assessment of the visualization efficiency of arbitrarily oriented SQEs, introducing the degree of orientational independence of the excitation rate

$$\varepsilon_{ex} = \frac{\max\left(\Gamma_{ex}^{\min}\right)}{\max\left(\Gamma_{ex}^{\max}\right)}, \tag{26}$$

where the excitation rate of a SQE Γ_{ex} is given by Eq. (9) for a linear dipole and by Eq. (10) for a 2D dipole; $\max(\Gamma_{ex}^{\min})$ and $\max(\Gamma_{ex}^{\max})$ are maximal values of the excitation rate of minimally and maximally excitable orientations, respectively. In Sec. IV, we will exploit both parameters ε_{im} and ε_{ex}.

C. Elliptically polarized cylindrical vector beams: Properties and tight focusing

1. Focusing equations for cylindrical vector beams

Two basic cylindrical vector beams—the radially and the azimuthally polarized beam—have been analyzed previously and are described in detail in [82]. In the present investigation we will perform simulations for cylindrical vector beams formed by Hermite-Gaussian modes HG_{10} and HG_{01} [75]. Previously, we have introduced the elliptically polarized cylindrical vector beam [36,40] and here we consider the laser excitation beam before the entrance of the microscope objective to have the following light field distribution:

$$\mathbf{E}_{in} = E_0 F(\theta)[(\sin\alpha)e^{i\Phi}\mathbf{n}_\rho + (\cos\alpha)e^{-i\Phi}\mathbf{n}_\varphi], \tag{27}$$

where

$$F(\theta) = \frac{2\sin\theta}{f_0\sin\theta_m}\exp\left(-\frac{1}{f_0^2}\frac{\sin^2\theta}{\sin^2\theta_m}\right). \tag{28}$$

Here f_0 is the filling factor, θ_m the angular aperture of the microscope objective, E_0 the amplitude of the light field, θ the polar angle of the spherical coordinate system with the origin in the geometrical focus of the microscope objective, $\mathbf{n}_\rho$ and $\mathbf{n}_\varphi$ the unit vectors of a cylindrical coordinate system, and α and Φ the amplitude ellipticity parameter and the phase ellipticity parameter, respectively. α and Φ are independent parameters and they are not functions of the spacial coordinates. The first term in the brackets of Eq. (27) represents the radially polarized mode [$\mathbf{E}_r = E_0 F(\theta)\mathbf{n}_\rho$] and the second term represents the azimuthally polarized mode [$\mathbf{E}_\varphi = E_0 F(\theta)\mathbf{n}_\varphi$]: both modes have the common amplitude represented by the multiplier before the brackets, the unit vectors assign radial ($\mathbf{n}_\rho$) and azimuthal ($\mathbf{n}_\varphi$) polarization distribution, α assigns the proportion between the radial and the azimuthal component, and Φ assigns the phase delay between the components.

Defining the laser beam focusing operator $\hat{F}$ as an operator that transforms an entrance laser beam into a focused beam, we can represent the focusing equations for radially and azimuthally polarized modes in the form

$$\hat{F}(\mathbf{E}_r) = Ae^{-ikf}[E_r(\rho,z)\mathbf{n}_\rho + E_z(\rho,z)\mathbf{n}_z], \tag{29a}$$

$$\hat{F}(\mathbf{E}_\varphi) = Ae^{-ikf}E_\varphi(\rho,z)\mathbf{n}_\varphi, \tag{29b}$$

with ρ and z being the cylindrical coordinates of the focal region, and $\mathbf{n}_\rho$, $\mathbf{n}_\varphi$, and $\mathbf{n}_z$ the respective unit vectors; the constant A reads as $A = -E_0 kf$; f is the focal distance of the microscope objective. The normalized complex amplitudes $E_r(\rho,z)$, $E_\varphi(\rho,z)$, and $E_z(\rho,z)$ are given by

$$E_\rho = \int_0^{\theta_m} F(\theta)J_1(kn\rho\sin\theta)h_-^p(\theta,z)(\cos\theta)^{3/2}\sin\theta d\theta, \tag{30a}$$

$$E_\varphi = -\int_0^{\theta_m} F(\theta)J_1(kn\rho\sin\theta)h_+^s(\theta,z)\sqrt{\cos\theta}\sin\theta d\theta, \tag{30b}$$

$$E_z = i\int_0^{\theta_m} F(\theta)J_0(kn\rho\sin\theta)h_+^p(\theta,z)\sqrt{\cos\theta}\sin^2\theta d\theta, \tag{30c}$$

where $J_n(x)$ is an nth-order Bessel function and the functions $h_\pm^{s(p)}$ read as

$$h_\pm^{s(p)}(\theta,z) = t_{l,out}^{s(p)}\frac{e^{ik_z nz} \pm r_{up,in}^{s(p)}(\theta)e^{ik_z n(L-z)}}{1 - r_{up,in}^{s(p)}(\theta)r_{l,in}^{s(p)}(\theta)e^{2ik_z nL}} \tag{31}$$

with $L = z_1 - z_2$ being the distance between the lower and the upper mirrors (see Fig. 4). So, combining Eqs. (27) and (29), we derive the following expression for the focused EPCVB:

$$\begin{aligned}\mathbf{E}_f = \hat{F}(\mathbf{E}_{in}) = Ae^{ikf}[&(\cos\alpha)e^{i\Phi}E_\rho(\rho,z)\mathbf{n}_\rho \\ &+ (\sin\alpha)e^{-i\Phi}E_\varphi(\rho,z)\mathbf{n}_\varphi + (\cos\alpha)e^{i\Phi}E_z(\rho,z)\mathbf{n}_z].\end{aligned} \tag{32}$$

Note that the amplitudes $E_\rho(\rho,z)$, $E_\varphi(\rho,z)$, and $E_z(\rho,z)$ are rotationally symmetric functions and do not depend on the azimuthal angle φ. In Sec. IV, we will assume the integration range in Eqs. (30) to be from 0 to 64° unless otherwise specified.

2. The interaction of a tightly focused EPCVB with a SQE

To simulate a LSCFM image of a linear dipole SQE, we need to calculate the multiplier $|\mathbf{E}(\mathbf{r})\cdot\mathbf{d}_a|^2$ in Eq. (6). Knowing the focal-region excitation-laser light field (32), we can express the absorption TDM unit vector in cylindrical coordinates and calculate the scalar product. The dipole unit vector is expressed as

$$\mathbf{d}_a = (\sin\theta_a\cos\phi)\mathbf{n}_\rho + (\sin\theta_a\sin\phi)\mathbf{n}_\varphi + (\cos\theta_a)\mathbf{n}_z \tag{33}$$

with

$$\phi = \varphi_a - \varphi. \tag{34}$$

Taking the scalar product of Eq. (33) with Eq. (32), we obtain for a linear dipole emitter

$$\begin{aligned}|\mathbf{E}_f(\mathbf{r})\cdot\mathbf{d}_a|^2 = {}& I_\rho(\rho,z)\cos^2\alpha\sin^2\theta_a\cos^2\phi + I_\varphi(\rho,z) \\ &\times \sin^2\alpha\sin^2\theta_a\sin^2\phi + I_z(\rho,z)\cos^2\alpha\cos^2\theta_a \\ &+ 0.5\big[I_{\rho\varphi}^r(\rho,z)\cos 2\Phi - I_{\rho\varphi}^i(\rho,z) \\ &\times \sin 2\Phi\big]\sin 2\alpha\sin^2\theta_a\sin 2\phi + I_{\rho z}^r(\rho,z) \\ &\times \cos^2\alpha\sin 2\theta_a\cos\phi + 0.5\big[I_{z\phi}^r(\rho,z)\cos 2\Phi \\ &- I_{z\phi}^i(\rho,z)\sin 2\Phi\big]\sin 2\alpha\sin 2\theta_a\sin\phi.\end{aligned} \tag{35}$$

For a 2D dipole SQE we have

$$
\begin{aligned}
&0.5\left[\left|\mathbf{E}(\mathbf{r})\cdot\mathbf{d}_1^{(abs)}\right|^2+\left|\mathbf{E}(\mathbf{r})\cdot\mathbf{d}_2^{(abs)}\right|^2\right]\\
&\quad=0.5I_\rho(\rho,z)\cos^2\alpha\\
&\qquad\times[\cos^2\theta_a\cos^2\phi+\sin^2\phi]+0.5I_\varphi(\rho,z)\sin^2\alpha\\
&\qquad\times[\cos^2\theta_a\sin^2\phi+\cos^2\phi]+0.5I_z(\rho,z)\cos^2\alpha\sin^2\theta_a\\
&\qquad-0.25\left\{I^r_{\rho\varphi}(\rho,z)\cos 2\Phi\ -I^i_{\rho\varphi}(\rho,z)\right.\\
&\qquad\left.\times\ \sin 2\Phi\right\}\sin 2\alpha\sin^2\theta_a\sin 2\phi-0.5I^r_{\rho z}(\rho,z)\\
&\qquad\times\ \cos^2\alpha\sin 2\theta_a\cos\phi-0.25\left\{I^r_{z\phi}(\rho,z)\cos 2\Phi\right.\\
&\qquad\left.-I^i_{z\phi}(\rho,z)\sin 2\Phi\right\}\sin 2\alpha\sin 2\theta_a\sin\phi,
\end{aligned}
\tag{36}
$$

where the light field intensity functions read as

$$I_\rho(\rho,z)=|E_\rho(\rho,z)|^2, \tag{37a}$$
$$I_\varphi(\rho,z)=|E_\varphi(\rho,z)|^2, \tag{37b}$$
$$I_z(\rho,z)=|E_z(\rho,z)|^2, \tag{37c}$$
$$I^r_{\rho\varphi}(\rho,z)=\mathrm{Re}[E_\rho(\rho,z)E^*_\varphi(\rho,z)], \tag{37d}$$
$$I^i_{\rho\varphi}(\rho,z)=\mathrm{Im}[E_\rho(\rho,z)E^*_\varphi(\rho,z)], \tag{37e}$$
$$I^r_{\rho z}(\rho,z)=\mathrm{Re}[E_\rho(\rho,z)E^*_z(\rho,z)], \tag{37f}$$
$$I^r_{z\varphi}(\rho,z)=\mathrm{Re}[E_z(\rho,z)E^*_\varphi(\rho,z)], \tag{37g}$$
$$I^i_{z\varphi}(\rho,z)=\mathrm{Im}[E_z(\rho,z)E^*_\varphi(\rho,z)]. \tag{37h}$$

Functions (37a), (37b), and (37c) represent the intensities of the radial, the azimuthal, and the longitudinal component of the focused laser light field, respectively; functions (37d) through (37h) represent the interference field components.

III. THEORETICAL ANALYSIS OF EPCVB-BASED LSCFM IMAGING OF SINGLE QUANTUM EMITTERS

To simulate the visualization of SQEs by means of EPCVB-based LSCFM, we first need to explore the formulas (30), (35), (36), and (37). Figure 6 displays functions (37) calculated for the excitation field focused into a polymer film supported by a glass slide as an example. The refractive indices of the glass and of the polymer are stated to be equal to 1.5, the film is 20-nm thick, and $n_{out}=1$ (the sample is surrounded by air). The figure displays the focused field at the polymer–glass interface, which is located 20 nm below the polymer–air interface. Other parameters are stated to be $(\theta_m, f_0, \lambda_{ex})=(64^\circ, 1{,}490\ \mathrm{nm})$. Analyzing Eqs. (35) and (36), we see that the ratio between the azimuthal focal field component I_φ and the components produced by the focusing of the radially polarized beam (I_ρ, I_z, and $I^r_{\rho z}$) can be readily controlled with the amplitude ellipticity parameter α. However, there appear terms created by the interference of the azimuthal component with the longitudinal and the radial components in Eqs. (35) and (36), reducing the controllability with α. These terms can be controlled with the phase ellipticity parameter Φ. As one can see in Fig. 6, the basic and the interference field components are of comparable magnitude in this example. Hence, the interference components (and due to this, the parameter Φ) do affect the arbitrarily oriented SQE visualization efficiency. In this example, the excitation OID

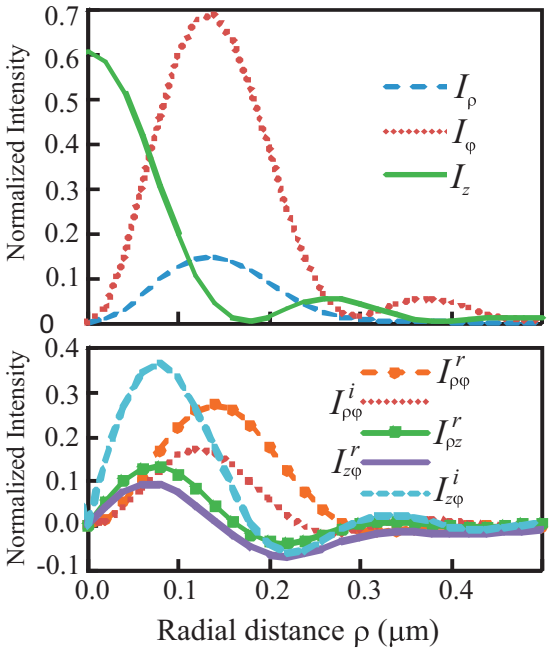

FIG. 6. An example of calculated excitation laser focal field components. The field is focused 20 nm below the polymer–air interface.

ε_{ex} (25) of a linear dipole SQE behaves as follows: for a radially polarized beam, $\varepsilon_{ex}=0.24$; for $\alpha=40^\circ$ and $\Phi=0$, $\varepsilon_{ex}=0.8$; for $\alpha=38.5^\circ$ and $\Phi=76^\circ$, we have $\varepsilon_{ex}=0.93$. Here, $\alpha=40^\circ$ provides the maximal value of ε_{ex} at $\Phi=0$, and the set $(\alpha,\Phi)=(38.5^\circ,76^\circ)$ provides the maximum possible value of ε_{ex}. A similar analysis of arbitrarily oriented SQE visualization in a homogeneous medium [36] gives $\varepsilon_{ex}=0.29$ for a radially polarized beam, $\varepsilon_{ex}=0.57$ for $(\alpha,\Phi)=(44.5^\circ,0)$, $\varepsilon_{ex}=0.94$ for $(\alpha,\Phi)=(47.5^\circ,28^\circ)$. Note that for a homogeneous medium the functions $I^r_{\rho z}$, $I^r_{z\varphi}$, and $I^i_{\rho\varphi}$ vanish in the focal plane of the microscope objective [$z=0$ in Eqs. (37)], which can be readily explained by the fact that at $z=0$ in a homogeneous medium the functions $h^{s(p)}_\pm$ in Eqs. (31) and (30) are equal to 1, making the integrals in Eqs. (30) real numbers. Comparing the controllability of the OID in these two examples, we conclude that there is a high controllability with the amplitude ellipticity parameter and not high controllability with the phase ellipticity parameter for SQEs under the polymer–air interface, but in the case of SQEs in a homogeneous medium the controllability with the phase parameter is of the same magnitude as the controllability with the amplitude parameter.

Further analysis of Eqs. (35) and (36) shows that the ratio between the components I_ρ, I_z, and $I^r_{\rho z}$ cannot be controlled with the ellipticity parameters. On the one hand, there are six independent functions among the intensities (37) and we obviously cannot perform a complete control over Eqs. (35) and (36) varying only two parameters. On the other hand, in the above-mentioned examples $\varepsilon_{ex}=0.93$ and $\varepsilon_{ex}=0.94$ have been reached and we have demonstrated previously that the degree of orientational independence higher than 0.9 can be reached for SQEs located in a homogeneous medium ($\varepsilon_{im}=0.96$) [36] and inside a 99%-collection-efficiency antenna [40]

($\varepsilon_{im} > 0.9$). These values are significantly high, taking into account that the maximal possible value of this parameter is $\varepsilon_{im} = 1$. So, we do not have a guarantee that the EPCVB-based LSCFM technique can provide a high OID for visualization of SQEs located in any layered medium, but there is a good probability to obtain a high degree and this problem can be studied for any layered medium.

In general, the visualization of arbitrarily oriented linear dipole SQEs is a challenging problem and to find an EPCVB providing the most efficient visualization, we need to explore Eqs. (35) and (1) numerically: this task cannot be solved analytically even for SQEs in a homogeneous medium. However, there are particular predictions about the field structure which must be satisfied to make an efficient arbitrarily oriented SQE visualization possible. As was mentioned above, the ratio between the functions I_ρ, I_z, and $I^r_{\rho z}$ is not controlled with the ellipticity parameters. At the same time, the longitudinal field component I_z excites z-oriented SQEs and the radial component I_ρ excites emitters with TDMs lying in the plane of a layered structure. Consequently, if we have a big radial component compared to the longitudinal one, it will be impossible to optimize the OIDs (25) and (26) with the ellipticity parameters [see Eq. (35)]. Nevertheless, the emitters with TDMs lying in the plane of a layered structure can be excited not only with the radial component, but also with the azimuthal component and the ratio between this and the longitudinal component is well controlled with the ellipticity parameters. So, for the visualization of arbitrarily oriented linear dipole SQEs to be successful, the EPCVB must satisfy the following two qualitative conditions: (I) the longitudinal component must be bigger in magnitude than the radial component, (II) the azimuthal component must not be equal to zero and it desirably should be of comparable magnitude with the longitudinal component.

The visualization of arbitrarily oriented 2D dipole SQEs is an easier task and it can be partially solved analytically. The analysis of Eq. (36) shows that the result for the degree of orientational independence of the excitation probability (26) with a radially polarized beam or a beam of mixed polarization is questionable, but with the azimuthally polarized beam $\varepsilon_{ex} = 1$ can be reached for any layered medium. To prove it, we will analyze the orientational dependence of the excitation rate for this case. Putting in Eq. (36) $(\alpha, \Phi) = (90^\circ, 0)$, we have

$$\Gamma^{2D}_{ex}(\mathbf{r}, \mathbf{d}_a) \propto I_\varphi(\rho, z)[\cos^2\theta_a \sin^2\phi + \cos^2\phi], \tag{38}$$

which means that the orientational dependence is defined by the function

$$F(\theta_a, \phi) = \cos^2\theta_a \sin^2\phi + \cos^2\phi = 1 - \sin^2\theta_a \sin^2\phi. \tag{39}$$

As the angles θ_a and ϕ are real numbers, the largest value of this function is equal to unity. Analyzing Eq. (39), we can see that the function takes on this value at $\sin\theta_a = 0$ or $\sin\phi = 0$. Hence, taking into account Eq. (34), the biggest possible value of the excitation rate of a 2D dipole emitter is reached at $\varphi_a = \varphi$ and $\varphi_a = \varphi + \pi$. Physically, it means that (at least) in two points of an image of arbitrarily oriented emitter the excitation rate reaches its maximum possible value and the degree of excitation rate orientational independence (26) is equal to unity. Figure 7 displays a set of images of 2D dipole SQEs of different orientations located in a polymer film ($n = 1.5$) 20 nm below the polymer–air interface as an example. The intrinsic quantum yield of the SQEs is stated to be equal to unity. In this example, the orientational dependence of the collection efficiency (7) is extremely weak (a variation of about 2% in the range $\theta_e = [0 \ldots 90^\circ]$) and the total quantum yield (8) does not depend on the orientation. The degrees of orientational independence ε_{ex} and ε_{im} are equal to 1 and 0.98, respectively. Analyzing Fig. 7, we see that the intensity maximum does not depend on the emitter's orientation, but the bright area of an image does depend on it. However, the smallest bright area (image of the emitter with $\theta_a = 90^\circ$) is comparable with the biggest bright area (image of the emitter with $\theta_a = 0^\circ$) and we suppose here that the difference in areas does not affect the visualization efficiency. Further, if the collection efficiency and the quantum yield of a 2D dipole SQE are not strongly affected by the emitting TDM orientation, the image intensity maximum OID—despite the fact that it should be evaluated numerically—will likely be maximized either with the azimuthally polarized beam or with a beam close to one that is azimuthally polarized.

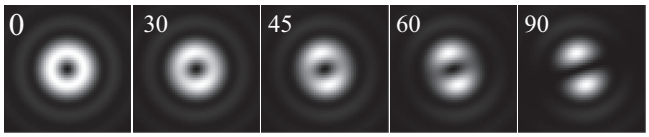

FIG. 7. Simulated LSCFM images of 2D dipole SQEs located in a polymer film ($n = 1.5$) 20 nm below the polymer–air interface; $\varphi_a = 17^\circ$. The numbers in the corners of the images represent the angle θ_a (deg).

IV. COMPUTER SIMULATIONS OF THE VISUALIZATION OF SINGLE QUANTUM EMITTERS NEAR PLANAR INTERFACES

A. Visualization of single quantum emitters on surfaces

It has been demonstrated previously that transparent and semitransparent surfaces can improve fluorescent properties of SQEs [46,48] and the technique of surface-enhanced fluorescence is widely used today [48]. This tool has been used for visualization of optically biased Brownian rotation of fluorescent surface-bound molecules [49], for studying the dynamics of polymer surfaces [47], and for some other applications [46,57,58,83]. So, in the present subsection we theoretically study the visualization of arbitrarily oriented SQEs located on surfaces that enhance their fluorescent properties.

1. SQEs on the surface of a glass slide

Here, we consider the visualization of SQEs located on the surface of a glass slide or a polymer film in air. The results of the simulations of the visualization of linear dipole SQEs are collected in Table I; similar results for 2D dipole emitters are collected in Table II. As was mentioned above, the total quantum yield Q of a SQE and the microscope objective collection efficiency η depend on the emitter's intrinsic quantum yield q_i and TDM orientation [Eqs. (8) and (7)]. So, we analyze

TABLE I. The results of simulations for the visualization of linear dipole SQEs on a glass slide; $\eta_{pl} = 0.71$, $\eta_z = 0.76$.

q_i	$\eta_{pl}Q_{pl}$	$\eta_z Q_z$	ε_r	$(\varepsilon_\alpha, \alpha)$	$(\varepsilon_{\alpha,\Phi}, \alpha, \Phi)$
1	0.71	0.76	0.09	(0.71, 61°)	(0.93, 60°, 74°)
0.5	0.41	0.53	0.08	(0.72, 64°)	(0.93, 63°, 74°)
$\to 0$	$0.99q_i$	$1.74q_i$	0.06	(0.74, 67°)	(0.91, 67°, 76°)
Excitation OID			0.1	(0.71, 61°)	(0.93, 60°, 72°)

the orientational-independent visualization of emitters with different intrinsic quantum yields: high q_i ($q_i = 1$), average q_i ($q_i = 0.5$), and low q_i ($q_i \to 0$). To see the influence of the emitting properties of a SQE on the visualization, we express the product ηQ in the tables. As before, the indices pl and z are associated with TDMs lying in the plane of a layered medium and normal to this plane, respectively. For both linear and 2D dipole we calculate the OID provided by the radially polarized excitation beam as the simplest EPCVB and the index r near ε's in the tables is associated with the radially polarized beam. For the linear dipole, we express the OID obtained with the EPCVB optimized with respect to the amplitude ellipticity parameter α at $\Phi = 0$ (α optimization, ε_α) and the OID obtained with the EPCVB optimized with respect to both ellipticity parameters [(α, Φ) optimization, $\varepsilon_{\alpha,\Phi}$] to compare these two optimizations. For a 2D dipole emitter, we do not express the similar OIDs in Table II as in this case the biggest OIDs are reached with the azimuthally polarized beam (ε_{az}). However, hereunder where appropriate we will express ε_α and $\varepsilon_{\alpha,\Phi}$ for 2D dipole emitters in other layered media.

According to the data presented in Tables I and II, the collection efficiency depends on the emission TDM orientation very slightly both for linear dipole and for 2D dipole emitters. The total quantum yield depends on the orientation significantly only for emitters with a low intrinsic quantum yield, but it depends slightly for emitters with an average intrinsic quantum yield and does not depend at all for emitters with a high q_i as there is no energy dissipation at this interface. For linear dipole SQEs the degree of orientational independence ranges from 0.91 to 0.93, depending on the emitters' intrinsic quantum yield. Optimizing the excitation beam only with respect to the amplitude ellipticity parameter α, one can reach a degree of orientational independence in the range from 0.71 to 0.74. So, the (α, Φ) optimization enhances the degree of orientational independence in this case, but less than for SQEs in a homogeneous medium. For 2D dipole emitters, the maximal value of the degree of orientational independence is reached with an azimuthally polarized excitation beam for any intrinsic quantum yield. For 2D dipole SQEs with a small q_i the degree of orientational independence is not significantly high in this case: it amounts to 0.73. The radially polarized excitation beam provides a small OID both for linear and 2D dipole emitters: it amounts to less than 0.1.

TABLE II. The results of simulations for the visualization of 2D dipole SQEs on a glass slide; $\eta_{pl} = 0.74$, $\eta_z = 0.71$, $\varepsilon^r_{ex} = 0.1$.

q_i	Q_{pl}	Q_z	$\eta_{pl}Q_{pl}$	$\eta_z Q_z$	ε_{az}	ε_r
1	1	1	0.74	0.71	0.97	0.1
0.5	0.65	0.58	0.48	0.41	0.87	0.09
$\to 0$	$1.85q_i$	$1.4q_i$	$1.37q_i$	$0.99q_i$	0.73	0.07

TABLE III. The results of simulations for the visualization of linear dipole SQEs near the plasmonic gold film; $\eta_{pl} = 0.47$, $\eta_z = 0.8$.

q_i	$\eta_{pl}Q_{pl}$	$\eta_z Q_z$	ε_r	$(\varepsilon_\alpha, \alpha)$	$(\varepsilon_{\alpha,\Phi}, \alpha, \Phi)$
1	0.16	0.38	0.2	(0.68, 81°)	(0.7, 84°, 80°)
0.5	0.1	0.34	0.23	(0.57, 85°)	(0.6, 85°, 78°)
$\to 0$	$0.28q_i$	$2.67q_i$	0.33	(0.35, 87°)	(0.36, 87°, 76°)
Excitation OID			0.11	(0.6, 83°)	(0.96, 82°, 59°)

2. *SQEs on top of plasmonic layered structures*

The simplest plasmonic layered medium is a thin metal film on a dielectric substrate. In relation to single-molecule microscopy, this structure was studied for the first time by Stefani *et al.* [52]. In their study, the authors observed the fluorescence of single dye molecules through a thin gold film on a glass substrate; the emission of the molecules was in resonance with surface plasmon modes. The molecules were separated from the metal film by a polymer spacer. It was demonstrated that under these conditions fluorescent properties of the molecules can be modified in a desirable way. In particular, the number of photons detectable from molecules with TDMs perpendicular to the film can be enhanced. Here, we investigate the visualization of arbitrarily oriented single molecules located on the top of such a plasmonic structure.

The excitation wavelength is stated to be $\lambda_{ex} = 633$ nm, the emission wavelength $\lambda_{em} = 670$ nm. The parameters of the plasmonic film are stated to be the following: the thickness of the polymer spacer $d_1 = 24$ nm, the thickness of the gold film $d_2 = 44$ nm, the refractive index of the polymer $n_{pol} = 1.52$ and of glass $n_0 = 1.5$, the refractive index of gold at the excitation wavelength $n_g^{ex} = 0.142 + 3.56i$ and at the emission wavelength $n_g^{em} = 0.14 + 3.87i$. The molecules are supposed to be located on the surface of the polymer spacer in air ($n = 1$). The results of the calculations are collected in Table III for linear dipole emitters and in Table IV for 2D dipole emitters.

One can see that for a linear dipole emitter an excitation OID as high as 0.96 can be reached. However, due to quite big difference between the collection functions ηQ of the vertical and the horizontal dipole emitters (see the second and the third columns of Table III), the image intensity maximum OID is not so high (the last column of the table). In this case, for all considered intrinsic quantum yields the (α, Φ) optimization of the

TABLE IV. The results of simulations for the visualization of 2D dipole SQEs on the plasmonic gold film; $\eta_{pl} = 0.754$, $\eta_z = 0.47$, $\varepsilon^r_{ex} = 0.11$.

q_i	Q_{pl}	Q_z	$\eta_{pl}Q_{pl}$	$\eta_z Q_z$	ε_r	ε_{az}	$(\varepsilon_{\alpha,\Phi}, \alpha, \Phi)$
1	0.45	0.34	0.34	0.16	0.05	0.48	(0.49, 84°, 18°)
0.5	0.37	0.22	0.28	0.1	0.04	0.37	(0.38, 84°, 18°)
$\to 0$	$1.96q_i$	$0.59q_i$	$1.48q_i$	$0.28q_i$	0.02	0.19	(0.19, 83°, 14°)

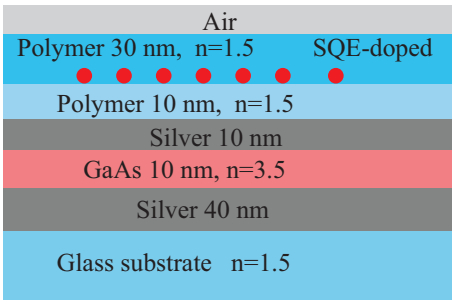

FIG. 8. The sketch of the layered plasmonic structure. The microscope objective is supposed to be located under the glass substrate.

excitation beam does not enhance the degree of orientational independence compared to the α optimization (compare the fifth and the sixth columns of Table III). The radially polarized beam provides optimal OID for small-q_i SQEs, but it does not work for average and high q_i's. Table IV shows that the orientational dependence of the product ηQ is strong for the 2D dipole emitter too and that optimal visualization efficiency is reached with the azimuthally polarized beam (compare columns 4 and 5). The radially polarized beam provides low OIDs: they amount to less than 0.05.

Further, we studied the visualization of SQEs located near the complicated metallo-dielectric planar plasmonic structure suggested and investigated in [62]. This structure is able to enhance fluorescence emission patterns and is attractive for single-molecule applications. The sketch and optical parameters of the considered structure are expressed in Fig. 8. We assume the excitation wavelength to be equal to 545 nm and the emission wavelength 565 nm as was suggested in [62]. Such absorption and emission wavelengths are characteristics, for example, of Rhodamine B molecules. The refractive index of silver is supposed to be equal to $0.05 + 3.53i$ at the absorption wavelength and $0.05 + 3.71i$ at the emission wavelength. The refractive indices of the other layers are supposed to be wavelength-independent and are expressed in Fig. 8.

The results of the simulations of the visualization of SQEs located in this structure are collected in Table V for linear dipole emitters and in Table VI for 2D dipole emitters. The radially polarized excitation beam provides low OIDs: from 0.05 to 0.12 depending on the intrinsic quantum yield of SQEs and the dimension of their TDMs. For linear dipole SQEs, the α optimization gives near-maximal OIDs varying from 0.71 to 0.89 for different q_i's. For 2D dipole SQEs, the azimuthally polarized beam provides near-maximal OIDs: from 0.49 to 0.78.

TABLE V. The results of simulations for the visualization of linear dipole SQEs on the top of plasmonic layered medium; $\eta_{pl} = 0.6$, $\eta_z = 0.89$.

q_i	$\eta_{pl} Q_{pl}$	$\eta_z Q_z$	ε_r	$(\varepsilon_\alpha, \alpha)$	$(\varepsilon_{\alpha,\Phi}, \alpha, \Phi)$
1	0.18	0.25	0.1	(0.86, 84°)	(0.9, 84°, 83°)
0.5	0.13	0.21	0.09	(0.87, 84°)	(0.92, 84°, 31°)
$\to 0$	$0.46q_i$	$1.4q_i$	0.05	(0.71, 86°)	(0.76, 86°, 36°)
Excitation OID			0.15	(0.89, 82°)	(0.91, 82°, 14°)

TABLE VI. The results of simulations for the visualization of 2D dipole SQEs on the top of plasmonic layered medium; $\eta_{pl} = 0.8$, $\eta_z = 0.6$, $\varepsilon^r_{ex} = 0.15$.

q_i	$\eta_{pl} Q_{pl}$	$\eta_z Q_z$	ε_r	ε_{az}	$(\varepsilon_{\alpha,\Phi}, \alpha, \Phi)$
1	0.23	0.18	0.12	0.78	(0.84,84°,61°)
0.5	0.18	0.13	0.1	0.7	(0.76, 84°, 61°)
$\to 0$	$0.45q_i$	$0.93q_i$	0.07	0.49	(0.54, 83°, 58°)

B. SQEs in a thin polymer film on a substrate

In this subsection, we will consider the visualization of arbitrarily oriented SQEs embedded in a polymer film supported by a transparent dielectric substrate. A well known and widely used example of such a system is a thin polymer film doped with fluorescent dye molecules, supported by a glass slide. In the literature, there have been reported films of the following thicknesses: 20 nm [29], 50 nm [7], 30 and 80 nm [34], 10–30 nm [84], and 20 nm [31]. Taking into account these examples, we theoretically study films of thicknesses from several nm to 100 nm.

1. Linear dipole SQEs in a supported polymer film

Figure 9 displays the products ηQ (collection functions) of linear dipole emitters lying in the plane of the sample (η_{pl} and Q_{pl}) and perpendicular to this plane (η_z and Q_z) as functions of the distance between an emitter and the polymer–air interface at different values of the intrinsic quantum yield. Low-q_i collection functions are normalized to the intrinsic quantum yield; high-q_i and average-q_i functions are not normalized. The collection function of in-plane dipoles depends weakly on the thickness of the film and depends very slightly on the intrinsic quantum yield. In contrast, the collection function of z-oriented dipoles depends strongly both on the intrinsic quantum yield and on the film thickness.

For SQEs with small and average intrinsic quantum yields ($q_i \to 0$ and $q_i = 0.5$) the collection function depends significantly on the emitter's TDM orientation at small film thicknesses. For $q_i \to 0$ this dependence is strong at the thicknesses less than 80 nm and for $q_i = 0.5$ for thicknesses less than 65 nm. At thicknesses bigger than the respective

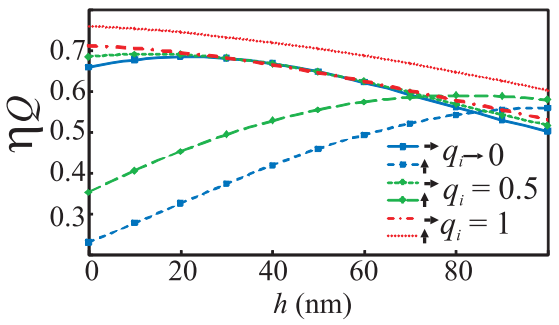

FIG. 9. The product ηQ of SQEs in a polymer film on a glass surface as a function of the distance from air–polymer interface at different intrinsic quantum yields q_i. Vertical and horizontal arrows are related to z-oriented and in-plane TDMs, respectively. The low-q_i curves are normalized to q_i.

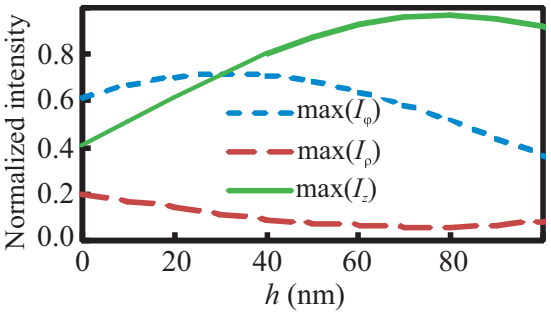

FIG. 10. Maximums of the intensities I_ρ, I_φ, and I_z as functions of the distance from the air–polymer interface h.

values and less than 100 nm, the dependence is not strong. That means that the visualization of arbitrarily oriented SQEs with small or average intrinsic quantum yield turns out to be a readily solvable task if the emitters are located under a quite thick film (>0.65 nm), but this task cannot be solved effectively for ultra-thin films (from several nm to 50 nm).

To perform further simulations of the visualization of arbitrarily oriented SQEs, we calculated the tightly focused excitation light field distribution inside the film. The maximal values of the radial, azimuthal, and longitudinal intensities (37a)–(37c) as functions of the distance from the polymer–air interface are depicted in Fig. 10. Here, the term maximal value means a maximal intensity in a plane with the respective longitudinal coordinate. The geometrical focus of the microscope objective is supposed to lie in the plane of the polymer–air interface.

The figure shows that the azimuthal and the longitudinal components are significantly greater in magnitude than the radial component, which gives rise to a good potential for optimizing the input beam with respect to the ellipticity parameters, working with SQEs lying in the same horizontal plane. However, the field intensities strongly depend on the longitudinal position, making the simultaneous visualization of SQEs located in different horizontal planes of the film inefficient. Figure 11 displays the OIDs of SQE visualization

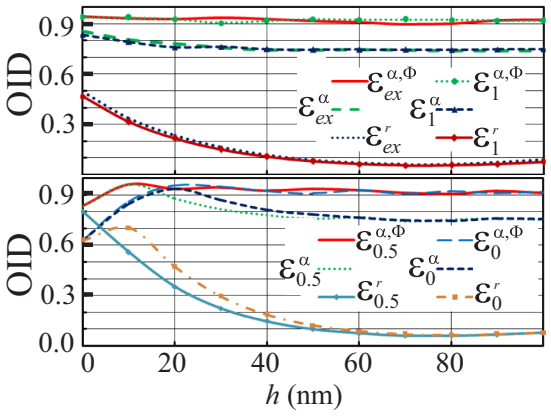

FIG. 11. The orientational independence degree as a function of a cover film thickness for SQEs with different intrinsic quantum yields. The upper indices near ε's denote the type of beam and the lower indices express SQEs' intrinsic quantum yield.

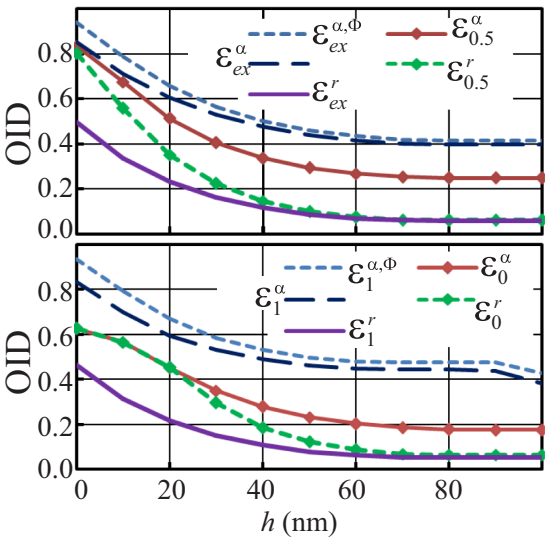

FIG. 12. The orientational independence degree as a function of the film thickness. SQEs are dispersed in the film. The upper indices near ε's denote the type of beam and the lower indices express SQEs' intrinsic quantum yield.

as functions of a polymer film thickness. Here, we consider the case when the emitters are localized on the glass surface and covered with a polymer film of an assigned thickness. As before, we compare two possible optimizations of the excitation beam: the optimization with respect to the amplitude ellipticity parameter α only at $\Phi = 0$ [see Eq. (27)] and the optimization with respect to both ellipticity parameters α and Φ. The figure shows that normally α optimization gives the degree of orientational independence about 0.7–0.75 and (α, Φ) optimization gives 0.9–0.95. The exception to this rule takes place for films thinner than 20 nm, covering emitters with small or average quantum yield: in this case the phase ellipticity parameter does not control the degree of orientational independence. It can be explained by the fact that the collection function of z-oriented emitters is significantly less than that function of in-plane emitters (see Fig. 9) and maximally efficient visualization of arbitrarily oriented SQEs is provided by the near-radially polarized beam. For thicker films, the radially polarized beam does not provide a high OID.

In the next step, we analyzed the visualization of emitters dispersed in the film (not localized on the polymer–glass interface as was considered above). Figure 12 displays the OIDs as functions of a film thickness. Here, the dimmest and the brightest emitters in Eqs. (25) and (26) were considered not only with respect to the TDM orientations, but also with respect to their longitudinal positions (z positions) in the film. As before, it is assumed that the geometrical focus of the microscope objective lies in the plane of the polymer–air interface and that no scan in the longitudinal direction is performed. The latter is reasonable as a film under consideration is quite thin (tens of nm).

In the range of film thicknesses from 1 nm to 100 nm the degree of orientational independence varies from 0.94 to 0.42 for high-q_i emitters, from 0.83 to 0.25 for average-q_i emitters, and from 0.62 to 0.18 for low-q_i emitters. The excitation OID varies from 0.85 to 0.4.

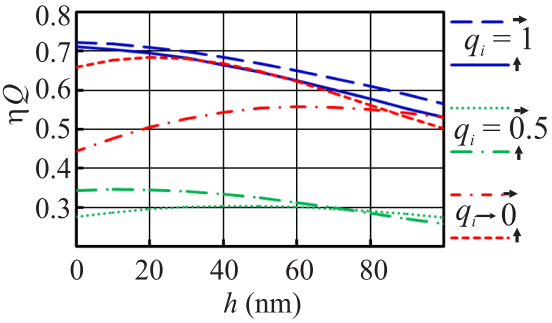

FIG. 13. The dependence of the product ηQ on the distance between the polymer–air interface and an emitter for 2D dipole SQEs with different intrinsic quantum yields q_i. The arrows are related to the emitters' orientations. The low-q_i curves are normalized to q_i.

2. 2D dipole SQEs in a supported polymer film

Figure 13 represents the product of the collection efficiency and the total quantum yield of a 2D dipole SQE as a function of the distance from the polymer–air interface. One can see that the smaller the intrinsic quantum yield is, the stronger the orientational dependence of the product becomes. Hence, the visualization of arbitrarily oriented SQEs can be effectively performed for emitters with a high q_i, but it can be less effectively performed for SQEs with a small q_i.

Figure 14 shows the orientational independence degrees of the visualization of arbitrarily oriented SQEs located on the glass–polymer interface. The degrees provided by an azimuthally polarized beam, by a radially polarized beam, by an α-optimized beam, and by an (α,Φ)-optimized beam are compared. For high quantum yield SQEs the three curves show almost the same behavior, which means that the highest degree of the orientational independence can be reached with azimuthally polarized excitation beam. However, for emitters with average and small intrinsic quantum yields in thin films the α optimization of the excitation beam enhances the degree

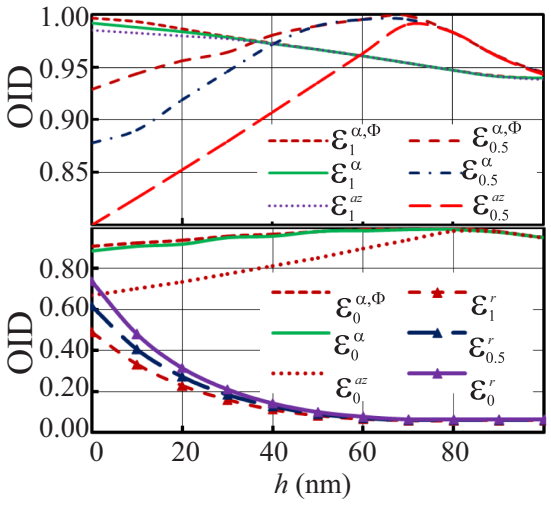

FIG. 14. The degree of orientational independence as a function of the cover film thickness for a 2D dipole SQE. The upper indices near ε's denote the type of beam and the lower indices express SQEs' intrinsic quantum yield.

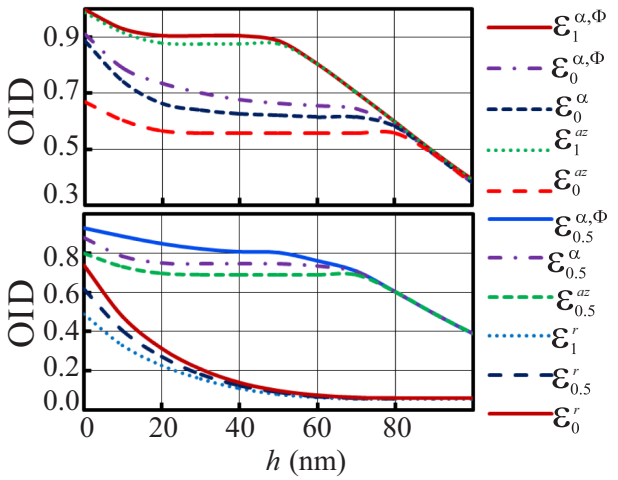

FIG. 15. The dependence of the degree of orientational independence on the thickness of a polymer film for a 2D dipole SQE. The emitters are dispersed in the film.

of orientational independence compared to an azimuthally polarized beam. The (α,Φ) optimization does not have any considerable advantage over the α optimization. The radially polarized beam provides optimal OIDs for low-q_i and average-q_i SQEs in ultrathin films, but it does not work for thicker films.

Figure 15 displays the OIDs as functions of a film thickness for emitters dispersed in the film. The maximal degree can be reached with the azimuthally polarized beam for high-q_i SQEs, but it can be enhanced by the α optimization for low- and average-q_i emitters. As before, the (α,Φ) optimization does not provide any significant enhancement and the radially polarized beam normally provides low OIDs, except for ultrathin films.

3. Enhanced visualization of arbitrarily oriented SQEs dispersed in a thin polymer film: The optimization of the microscope objective focus position

As has been shown earlier, for SQEs dispersed in a polymer film, the emitter's image intensity is sensitive to the emitter's longitudinal coordinate. It is caused by the rather high variation of the collection function of a SQE in the considered range of the longitudinal coordinates (Figs. 9 and 13) and by the strong dependence of the intensities of the focal-region light field components on the longitudinal coordinate (Fig. 10). The first condition cannot be controlled by the excitation beam, but the second one can. Both of these conditions cannot be controlled by the ellipticity parameters of the excitation beam. However, the problem can be solved, for example, by scanning a sample in the longitudinal dimension in addition to the scan in the plane of a film. Another possible solution to this problem is 2D scanning in the plane of a film at optimized position of the microscope objective geometrical focus, the position at which the variation of the intensities of the focal-region light field components in the longitudinal direction will be the least possible. Here, we will demonstrate such a solution.

To find an optimal position of the geometrical focus, we analyzed the stability of the ratio of the maximum of the longitudinal field component to the maximum of the azimuthal one $r = \max(I_z)/\max(I_\varphi)$. The maximums are taken in a plane

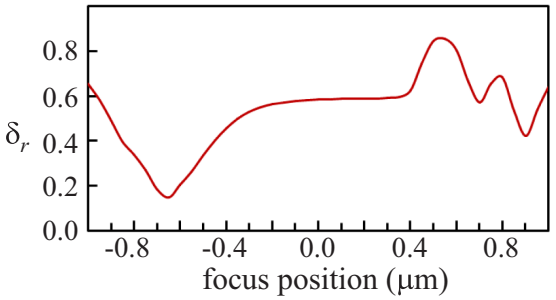

FIG. 16. The variation of the ratio of the intensity of the longitudinal focal-region light field component to the intensity of the azimuthal component as a function of the geometrical focus position.

of the film at a given longitudinal coordinate z. As a measure of the instability of the ratio, we exploit the following variation:

$$\delta_r = \frac{r_{max} - r_{min}}{r_{max} + r_{min}}, \tag{40}$$

where r_{max} and r_{min} are maximal and minimal values of the ratio in the range of the longitudinal coordinate from 0 to 0.1 μm. The smaller the variation is, the more stable the ratio will be: the optimal position of the geometrical focus corresponds to the smallest variation. Figure 16 shows the dependence of the variation on the position of the geometrical focus.

The variation takes on the smallest values at the position of the focus from -0.8 μm to -0.6 μm. The coordinate axis is directed as shown in Fig. 4 and the coordinate origin is located on the polymer–air interface. Thus, negative values of the longitudinal coordinate correspond to the geometrical focus located in air over the interface; the values from 0 to 0.1, to the focus in the polymer film (for 0.1-μm-thick films); the values greater than 0.1, to the focus in glass. Figure 17 is a detailed graph of the variation in the range of z_f from -0.75 μm to -0.55 μm. The minimum of the variation corresponds approximately to $z_f = -0.66$ μm, which gives us the optimal z_f.

Figure 18 displays in-plane maximums of the intensities of the focal-region field components at $z_f = -0.66$ μm. Comparing Figs. 10 and 18, we conclude that the intensity maximums are significantly more stable at $z_f = -0.66$ μm than at $z_f = 0$ and they are of comparable magnitude at

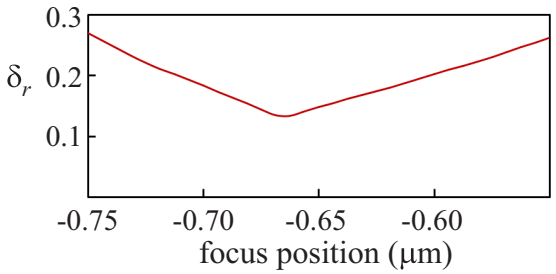

FIG. 17. The variation of the ratio of the intensity of the longitudinal focal-region light field component to the intensity of the azimuthal component as a function of the geometrical focus position: the local minimum.

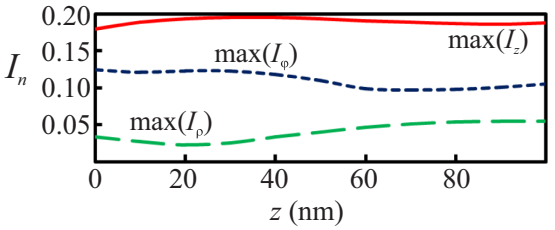

FIG. 18. Maximums of the intensities of the focal-region light field components at the geometrical focus position 660 nm above the polymer–air interface. I_n is the normalized intensity.

$z_f = -0.66$ μm and $z_f = 0$. At $z_f = -0.66$ μm the variation amounts to 0.14 and at $z_f = 0$ it amounts to 0.59.

Figure 19 displays the lateral dependence of the focal-region light field components at $z_f = -0.66$ μm and $z = 0.05$ μm (this value of z-coordinate corresponds to the middle plane of the polymer film). The components $I^r_{\rho z}$ and $I^i_{\rho\varphi}$ are not shown as they are small. The comparison of Fig. 19 and Fig. 6 brings us to the conclusion that the lateral area of the light field of the longitudinal component is not extended by the changing of the geometrical focus position, but the azimuthal component shows two bright maximums at $z_f = -0.66$ and the lateral dimension of this component is significantly enlarged. It makes the resolution of the LSCFM system lower, but this is not a significant drawback for applications in which polymer films containing ultrasmall concentrations of impurity molecules are exploited. On the other hand, the resolution is normally enhanced with a pinhole, which is not considered in the present paper. We have analyzed the same graphs for different lateral planes throughout the 0.1-μm-thick film and found out that the variations of the behavior of the field functions is small. So, we assumed $z_f = -0.66$ μm to be an optimal position of the geometrical focus and analyzed the visualization of arbitrarily oriented SQEs dispersed in a film at this position. The degree of orientational independence as a function of the film thickness for emitters with different q_i's at $z_f = -0.66$ μm is shown in Fig. 20. For films of less than 10 nm thicknesses the excitation OID is several percent smaller at $z_f = -0.66$ μm than at $z_f = 0$,

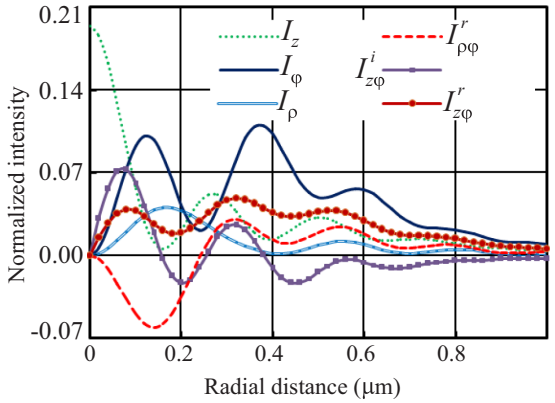

FIG. 19. The focal-region light field components in the middle of the film ($z = 50$ nm) for the geometrical focus position 0.66 μm above the polymer–air interface.

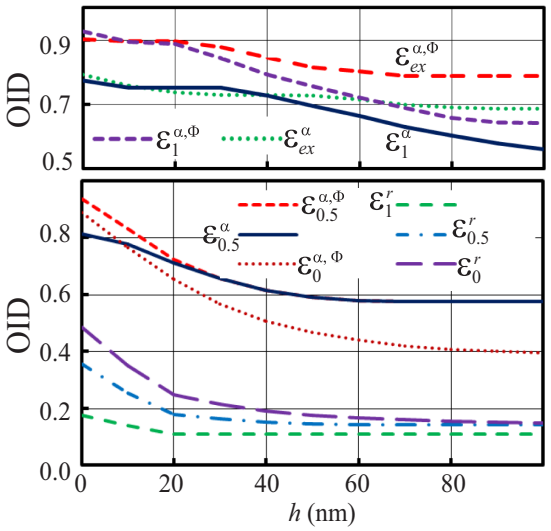

FIG. 20. The orientational independence degree as a function of a polymer film thickness for linear dipole SQEs. The emitters are dispersed in the film. The focus position is located 0.66 μm above the polymer–air interface.

but for thicker films there is an obvious advantage in OIDs at $z_f = -0.66$. In particular, for 0.1-μm-thick film we have $\varepsilon_{ex} = 0.78$ at $z_f = -0.66$ μm instead of $\varepsilon_{ex} = 0.42$ that takes place at $z_f = 0$. Again, the radially polarized excitation beam fails to provide efficient visualization of arbitrarily oriented SQEs. Figure 21 represents the degrees of orientational independence of the image intensity maximums for 2D dipole emitters as functions of the film thickness. We do not display (α,Φ)-optimized OIDs as these curves are very close to α-optimized OIDs. For high-q_i SQEs the maximal OID is provided by the azimuthally polarized beam; for average-q_i and low-q_i SQEs the α optimization enhances the OID up to 10% compared to the azimuthally polarized beam. OIDs provided by the radially polarized beam amount to less than 0.2.

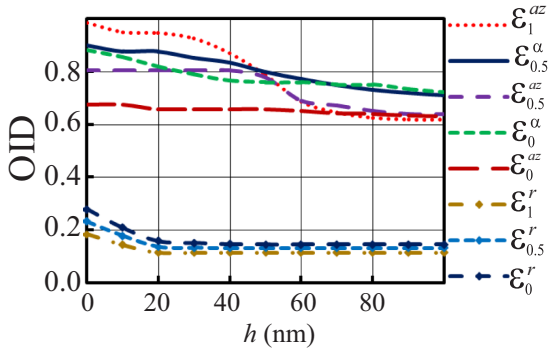

FIG. 21. The orientational independence degree as a function of a polymer film thickness for 2D dipole SQEs. The emitters are dispersed in the film. The focus position is located 0.66 μm above the polymer–air interface.

C. Visualization of arbitrarily oriented SQEs in cavity-like planar structures

In this subsection we consider the structure depicted in Fig. 3, in which both upper and lower mirrors are present and these two planar mirrors affect the excitation light field and SQEs' fluorescence like a Fabry-Pérot microcavity [85]. We study the following two structures of this type: a thin freestanding polymer film doped with dye molecules and a dielectric microcavity with an air layer between the planar mirrors.

1. SQEs in a freestanding polymer film

A planar polymer film of a stated thickness surrounded by air is studied. The description of such samples can be found, for example, in [71]. We explore freestanding films of two thicknesses—10 nm and 30 nm—as examples. For 10-nm-thick film we have the following focal-region light field intensity maximums [see Eqs. (37)]: $\max(I_\rho) = 0.15$, $\max(I_\varphi) = 0.29$, $\max(I_z) = 0.09$. The integration range in Eq. (30) was supposed to be from 0 to 64°. As the maximal value of the focal-region radially polarized component is about twice as large as the longitudinal component, the visualization of arbitrarily oriented SQEs cannot be performed efficiently. For this reason, we tried the simulation with annular illumination [29], making the integration range from 45° to 64°. It provided $\max(I_\rho) = 0.023$, $\max(I_\varphi) = 0.068$, $\max(I_z) = 0.027$. The intensities were reduced 3–4 times, but the longitudinal component exceeds the radial component, which provides an opportunity to control the excitation beam with the ellipticity parameters. Hereunder, we consider the visualization with this annular illumination.

The results of simulations of an arbitrarily oriented linear dipole SQE visualization for a 10-nm-thick film are collected in Table VII. This table and other tables of the present subsection are organized in the same way as in Sec. IV A. For the excitation OID we have a value as high as 0.58 for the α-optimized beam and 0.97 for the (α,Φ)-optimized beam, but for the image intensity maximum OID for high quantum yield emitters we have 0.58 and 0.69, respectively. This means that the optimization of the beam with respect to the phase ellipticity parameter increases the visualization efficiency by about 17%. This is caused by the strong orientational dependence of the collection function ηQ. For SQEs with average and small intrinsic quantum yields, we have $\varepsilon_{im} = 0.2$ and $\varepsilon_{im} = 0.13$, respectively, with the radially polarized beam and the (α,Φ) optimization does not provide any enhancement. So, in this case, the radially polarized excitation beam provides maximal

TABLE VII. The results of simulations for the visualization of linear dipole SQEs in a 10-nm-thick freestanding polymer film; $\eta_{pl} = 0.35$, $\eta_z = 0.21$.

q_i	$\eta_{pl}Q_{pl}$	$\eta_z Q_z$	ε_r	$(\varepsilon_\alpha, \alpha)$	$(\varepsilon_{\alpha,\Phi}, \alpha, \Phi)$
1	0.35	0.21	0.58	(0.58, 0°)	(0.69, 17°, 45°)
0.5	0.13	0.02	0.2	(0.2, 0°)	(0.2, 0°, 0°)
$\to 0$	$0.21q_i$	$0.025q_i$	0.13	(0.13, 0°)	(0.13, 0°, 0°)
Excitation OID			0.54	(0.58, 13°)	(0.97, 28°, 41°)

TABLE VIII. The results of simulations for the visualization of 2D dipole SQEs in a 10-nm-thick freestanding polymer film; $\eta_{pl} = 0.33$, $\eta_z = 0.35$, $\varepsilon_r^{ex} = 0.81$.

q_i	$\eta_{pl}Q_{pl}$	$\eta_z Q_z$	ε_r	ε_{az}	$(\varepsilon_\alpha, \alpha)$	$(\varepsilon_{\alpha,\Phi}, \alpha, \Phi)$
1	0.33	0.35	0.87	0.94	(0.98, 30°)	(0.99, 30°, 2°)
0.5	0.088	0.133	0.82	0.66	(0.82, 0°)	(0.82, 0°, 0°)
→ 0	$0.12q_i$	$0.21q_i$	0.69	0.56	(0.69, 0°)	(0.69, 0°, 0°)

TABLE X. The results of simulations for the visualization of 2D dipole SQEs in a 30-nm-thick freestanding polymer film; $\eta_{pl} = 0.36$, $\eta_z = 0.38$, $\varepsilon_r^{ex} = 0.81$.

q_i	$\eta_{pl}Q_{pl}$	$\eta_z Q_z$	ε_r	ε^{az}	$(\varepsilon_\alpha, \alpha)$	$(\varepsilon_{\alpha,\Phi}, \alpha, \Phi)$
1	0.36	0.38	0.86	0.73	(0.96, 30°)	(0.99, 33°, 6°)
0.5	0.085	0.13	0.81	0.65	(0.81, 0°)	(0.81, 0°, 0°)
→ 0	$0.11q_i$	$0.2q_i$	0.7	0.57	(0.70, 0°)	(0.7, 0°, 0°)

intensity image maximum OID for low-q_i and average-q_i SQEs and near-maximal OID for high-q_i SQEs.

Similar data for 2D dipole emitters is collected in Table VIII. The general conclusion for this data is that the (α, Φ) optimization does not enhance the OID compared to the α optimization and the azimuthally polarized beam fails to provide a maximal possible image intensity maximum OID. A radially polarized excitation beam provides higher OIDs than an azimuthally polarized one for low-q_i and average-q_i SQEs and these OIDs turn out to be maximal. For high-q_i SQEs, the azimuthally polarized beam provides an OID higher by about 7% than the radially polarized beam does. Thus, the radially polarized beam turns out to be optimal for maximizing image intensity maximum OID for SQEs located in 10-nm-thick freestanding film. However, the excitation OID can be significantly enhanced by the (α, Φ) optimization for linear dipole SQEs and it can be increased up to unity with the azimuthally polarized beam for 2D dipole emitters.

The data for 30-nm-thick films are presented in Tables IX and X. The results have some quantitative differences with those for 10-nm-thick film, but qualitatively the behavior of the collection functions and of the OIDs is the same for films of both thicknesses.

2. SQEs in a dielectric planar microcavity

Here, we study the microcavity suggested and described in [66]. It is formed by two dielectric mirrors: a high-reflective and a low-reflective one. In contrast to a freestanding polymer film, the inside of this microcavity is filled with air, creating smaller optical density inside the microcavity than outside. The simulations have been performed for the cavity of the following configuration: $n_{up} = (1.49, [n_1, n_2]_{\times 16}, n_1)$, $d_{up} = (0.025, [d_1, d_2]_{\times 16}, 0.1171)$ μm, $n_l = (n_2, [n_1, n_2]_{\times 4})$, $d_l = (d_4, [d_3, d_4]_{\times 4})$ μm, where $n_1 = 1.476121$, $n_2 = 2.384291$, $d_1 = 0.1101$, $d_2 = 0.0753$, $d_3 = 0.1137$, $d_4 = 0.0731$; the distance between the mirrors was stated to be $t = 0.135$ μm, and the SQEs were supposed to be located on the bottom of the upper (high-reflective) mirror.

The obtained data are collected in Tables XI and XII. In this case, the α optimization provides near-maximal OIDs both for linear and 2D dipole emitters. The radially polarized beam provides small OIDs, which amount to less than 0.23.

TABLE IX. The results of simulations for the visualization of linear dipole SQEs in a 30-nm-thick freestanding polymer film; $\eta_{pl} = 0.39$, $\eta_z = 0.23$.

q_i	$\eta_{pl}Q_{pl}$	$\eta_z Q_z$	ε_r	$(\varepsilon_\alpha, \alpha)$	$(\varepsilon_{\alpha,\Phi}, \alpha, \Phi)$
1	0.39	0.23	0.58	(0.58, 0°)	(0.71, 20°, 49°)
0.5	0.13	0.02	0.21	(0.21, 0°)	(0.21, 0°, 0°)
→ 0	$0.2q_i$	$0.025q_i$	0.15	(0.15, 0°)	(0.15, 0°, 0°)
Excitation OID			0.55	(0.6, 15°)	(0.97, 30°, 45°)

TABLE XI. The results of simulations for the visualization of linear dipole SQEs in a dielectric microcavity; $\eta_{pl} = 0.71$, $\eta_z = 0.27$.

q_i	$\eta_{pl}Q_{pl}$	$\eta_z Q_z$	ε_r	$(\varepsilon_\alpha, \alpha)$	$(\varepsilon_{\alpha,\Phi}, \alpha, \Phi)$
1	0.71	0.27	0.23	(0.91, 78°)	(0.95, 79.7°, 37°)
0.5	0.39	0.13	0.17	(0.9, 80°)	(0.93, 81°, 37°)
→ 0	$0.84q_i$	$0.7q_i$	0.1	(0.88, 82.7°)	(0.92, 82.7°, 85°)
Excitation OID			0.09	(0.87, 83.3°)	(0.94, 83.7°, 40°)

V. SUMMARY AND CONCLUSIONS

We have studied theoretically and analyzed numerically laser-scanning confocal fluorescence microscopy using an elliptically polarized cylindrical excitation vector beam as a tool for visualization of arbitrarily oriented single quantum emitters located (1) near surfaces enhancing fluorescence, (2) in a thin polymer supported film, (3) in thin freestanding polymer films, and (4) in a planar dielectric microcavity. Some properties of tightly focused EPCVBs within this task have been derived analytically. The orientational independence degree of LSCFM image intensity maximum and the orientational independence degree of the excitation probability were used as figures of merit of the visualization efficiency.

First, it has been shown that for SQEs, which absorb light as 2D dipoles, the highest possible OID equal to unity can be reached with an azimuthally polarized tightly focused excitation beam in LSCFM. It means that under conditions when the fluorescence collection efficiency of the microscope objective and the SQE's total quantum yield are not strongly orientational-dependent, the most efficient visualization of arbitrarily oriented 2D dipole SQEs can be accomplished with azimuthally polarized beams and normally azimuthally polarized beams are optimal for the visualization of such emitters. Exceptions to this rule take place for several-nm-thick supported polymer films doped with low-intrinsic-quantum-yield SQEs and for thin freestanding polymer films as in these examples the collected fluorescence power strongly depends on the emitters' TDM orientations. In all considered examples of the visualization of 2D dipole SQEs, the α optimization of EPCVB provides nearly maximal OID and the (α, Φ) optimization does not provide any significant enhancement of

TABLE XII. The results of simulations for the visualization of 2D dipole SQEs in a dielectric microcavity; $\eta_{pl} = 0.41$, $\eta_z = 0.71$, $\varepsilon^r_{ex} = 0.09$.

q_i	$\eta_{pl} Q_{pl}$	$\eta_z Q_z$	ε_r	ε_{az}	$(\varepsilon_\alpha, \alpha)$	$(\varepsilon_{\alpha,\Phi}, \alpha, \Phi)$
1	0.41	0.71	0.15	0.57	(0.9, 80.7°)	(0.96, 81°, 26°)
0.5	0.27	0.39	0.13	0.69	(0.92, 82°)	(0.97, 82°, 16°)
$\to 0$	$0.78q_i$	$0.84q_i$	0.09	0.92	(0.97, 84.7°)	(0.98, 84.7°, 3°)

the OID compared to the α optimization (the enhancement is less than 10%).

Second, we have studied the visualization of arbitrarily oriented linear dipole SQEs. This task is sophisticated and cannot be completely solved analytically. However, for the visualization to be successful, the following common condition should be satisfied: the longitudinal focal-region light field component of a tightly focused radially polarized excitation beam should be of greater magnitude than the radial focal-region component. Under this condition, one can control the ratio between the amplitudes of the longitudinal and the azimuthal focal-region components with the amplitude ellipticity parameter and the interference between these components can be controlled with the phase ellipticity parameter. It allows the excitation OID to reach values higher than 0.9. The image maximum OID is normally high for high-intrinsic-quantum-yield SQEs and low for low-intrinsic-quantum-yield SQEs, except for SQEs in a dielectric microcavity. Note that for linear dipole SQEs the (α, Φ) optimization of EPCVBs is more efficient than the α optimization and can enhance the OID, for example, from 0.6 up to 0.96.

Third, we have studied the opportunity of visualization of arbitrarily oriented SQEs dispersed in a polymer supported film of thicknesses up to 100 nm within one xy scan. The simulations have shown that the focal-region light field distribution depends on the longitudinal position of the microscope objective geometrical focus significantly. Finding the optimal position, one can minimize the dependence of the absolute values of the in-film focal-region field components on the longitudinal coordinate. We have found the position at which maximal variation of the field components amounts to less than 15%. It allows the OID to reach values higher than 0.78 for emitters dispersed in a supported film of thicknesses up to 100 nm.

So, we have demonstrated the applicability of the EPCVB-based LSCFM technique for visualization of arbitrarily oriented SQEs located near different planar interfaces and generally one can obtain a high OID if the collected fluorescence power is not significantly TDM-orientation-dependent.

ACKNOWLEDGMENTS

This work was supported by the Siberian Branch of the Russian Academy of Sciences (Project No. II.10.1.2). The author thanks Prof. A. V. Naumov and Prof. Yu. G. Vainer from the Institute for Spectroscopy of the Russian Academy of Sciences for discussions and wise recommendations related to the subject matter of the present paper.

[1] W. E. Moerner, Angew. Chem. Int. Ed. **54**, 8067 (2015).
[2] N. G. Walter, C.-Y. Huang, A. J. Manzo, and M. A. Sobhy, Nat. Methods **5**, 475 (2008).
[3] E. Betzig, G. H. Patterson, R. Sougrat, O. W. Lindwasser, S. Olenych, J. S. Bonifacino, M. W. Davidson, J. Lippincott-Schwartz, and H. F. Hess, Science **313**, 1642 (2006).
[4] W. R. Legant, L. Shao, J. B. Grimm, T. A. Brown, D. E. Milkie, B. B. Avants, L. D. Lavis, and E. Betzig, Nat. Methods **13**, 359 (2016).
[5] M. J. Rust, M. Bates, and X. Zhuang, Nat. Methods **3**, 793 (2006).
[6] S. Saurabh, A. M. Perez, C. J. Comerci, L. Shapiro, and W. E. Moerner, J. Am. Chem. Soc. **138**, 10398 (2016).
[7] A. M. Chizhik, R. Jäger, A. I. Chizhik, S. Bär, H.-G. Mack, M. Sackrow, C. Stanciu, A. Lyubimtsev, M. Hanack, and A. J. Meixner, Phys. Chem. Chem. Phys. **13**, 1722 (2011).
[8] A. V. Naumov, Phys. Usp. **56**, 605 (2013).
[9] T. Cordes and S. A. Blum, Nat. Chem. **5**, 993 (2013).
[10] B. Lounis and W. E. Moerner, Nature (London) **407**, 491 (2000).
[11] W. Moerner, New J. Phys. **6**, 88 (2004).
[12] B. Lounis and M. Orrit, Rep. Prog. Phys. **68**, 1129 (2005).
[13] S. Lukishova, A. Schmid, R. Knox, P. Freivald, L. J. Bissell, R. Boyd, C. Stroud Jr., and K. Marshall, J. Mod. Opt. **54**, 417 (2007).
[14] M. Steiner, A. Hartschuh, R. Korlacki, and A. J. Meixner, Appl. Phys. Lett. **90**, 183122 (2007).
[15] S. Castelletto, B. Johnson, V. Ivády, N. Stavrias, T. Umeda, A. Gali, and T. Ohshima, Nat. Mater. **13**, 151 (2014).
[16] A. Lohrmann, B. Johnson, J. McCallum, and S. Castelletto, Rep. Prog. Phys. **80**, 034502 (2017).
[17] Y. Chen, H. Lin, M. J. Ludford-Menting, A. H. Clayton, M. Gu, and S. M. Russell, Histochem. Cell Biol. **143**, 11 (2015).
[18] M. P. Backlund, M. D. Lew, A. S. Backer, S. J. Sahl, and W. Moerner, ChemPhysChem **15**, 587 (2014).
[19] D. Torchinsky and Y. Ebenstein, Nucleic Acids Res. **44**, e17 (2016).
[20] F. Fricke, J. Beaudouin, R. Eils, and M. Heilemann, Sci. Rep. **5**, 14072 (2015).
[21] A. S. Backer, M. Y. Lee, and W. Moerner, Optica **3**, 659 (2016).
[22] H. Sosa, E. J. Peterman, W. Moerner, and L. S. Goldstein, Nat. Struct. Mol. Biol. **8**, 540 (2001).
[23] A. Naumov, I. Y. Eremchev, and A. A. Gorshelev, Eur. Phys. J. D **68**, 348 (2014).
[24] D. J. Scardino, R. Kota, D. L. Mattern, and N. I. Hammer, Chem. Phys. Lett. **550**, 138 (2012).
[25] H. Piwoński, A. Sokołowski, M. Kijak, S. Nonell, and J. Waluk, J. Phys. Chem. Lett. **4**, 3967 (2013).
[26] P. Fita, L. Grill, A. Listkowski, H. Piwoński, S. Gawinkowski, M. Pszona, J. Sepioł, E. Mengesha, T. Kumagai, and J. Waluk, Phys. Chem. Chem. Phys. **19**, 4921 (2017).
[27] E. Betzig and R. J. Chichester, Science **262**, 1422 (1993).
[28] J. Sepioł, J. Jasny, J. Keller, and U. P. Wild, Chem. Phys. Lett. **273**, 444 (1997).
[29] B. Sick, B. Hecht, and L. Novotny, Phys. Rev. Lett. **85**, 4482 (2000).

[30] L. Novotny, M. R. Beversluis, K. S. Youngworth, and T. G. Brown, Phys. Rev. Lett. **86**, 5251(R) (2001).

[31] A. Debarre, R. Jaffiol, C. Julien, D. Nutarelli, A. Richard, P. Tchénio, F. Chaput, and J.-P. Boilot, Eur. Phys. J. D **28**, 67 (2004).

[32] M. R. Beversluis, L. Novotny, and S. J. Stranick, Opt. Express **14**, 2650 (2006).

[33] M. Reuss, J. Engelhardt, and S. W. Hell, Opt. Express **18**, 1049 (2010).

[34] H. Ishitobi, I. Nakamura, N. Hayazawa, Z. Sekkat, and S. Kawata, J. Phys. Chem. B **114**, 2565 (2010).

[35] X. Wang, S. Chang, L. Lin, L. Wang, and S. Hao, Optik **122**, 773 (2011).

[36] S. Boichenko and E. F. Martynovich, J. Exp. Theor. Phys. **97**, 52 (2013).

[37] V. Lotito, U. Sennhauser, C. V. Hafner, and G.-L. Bona, Prog. Electromagn. Res. **121**, 281 (2011).

[38] R. Gutbrod, D. Khoptyar, M. Steiner, A. M. Chizhik, A. I. Chizhik, S. Bär, and A. J. Meixner, Nano Lett. **10**, 504 (2010).

[39] P. R. Dolan, X. Li, J. Storteboom, and M. Gu, Opt. Express **22**, 4379 (2014).

[40] S. Boichenko and K. König, J. Opt. Soc. Am. B **32**, 601 (2015).

[41] R. Noriega, E. S. Barnard, B. Ursprung, B. L. Cotts, S. B. Penwell, P. J. Schuck, and N. S. Ginsberg, J. Am. Chem. Soc. **138**, 13551 (2016).

[42] D. Wöll, E. Braeken, A. Deres, F. C. De Schryver, H. Uji-i, and J. Hofkens, Chem. Soc. Rev. **38**, 313 (2009).

[43] H. Ishitobi, T. Kai, K. Fujita, Z. Sekkat, and S. Kawata, Chem. Phys. Lett. **468**, 234 (2009).

[44] R. Vallée, M. Van der Auweraer, W. Paul, and K. Binder, Europhys. Lett. **79**, 46001 (2007).

[45] R. Vallée, W. Paul, and K. Binder, J. Chem. Phys. **127**, 154903 (2007).

[46] E. Fort and S. Grésillon, J. Phys. D: Appl. Phys. **41**, 013001 (2007).

[47] G. Zhang, L. Xiao, F. Zhang, X. Wang, and S. Jia, Phys. Chem. Chem. Phys. **12**, 2308 (2010).

[48] T. Ruckstuhl, J. Enderlein, S. Jung, and S. Seeger, Anal. Chem. **72**, 2117 (2000).

[49] J. A. Hutchison, H. Uji-i, A. Deres, T. Vosch, S. Rocha, S. Müller, A. A. Bastian, J. Enderlein, H. Nourouzi, C. Li *et al.*, Nat. Nanotechnol. **9**, 131 (2014).

[50] H. Blom, A. Chmyrov, K. Hassler, L. M. Davis, and J. Widengren, J. Phys. Chem. A **113**, 5554 (2009).

[51] H. Yokota, K. Saito, and T. Yanagida, Phys. Rev. Lett. **80**, 4606 (1998).

[52] F. D. Stefani, K. Vasilev, N. Bocchio, N. Stoyanova, and M. Kreiter, Phys. Rev. Lett. **94**, 023005 (2005).

[53] J. Enderlein and T. Ruckstuhl, Opt. Express **13**, 8855 (2005).

[54] J. R. Lakowicz, Anal. Biochem. **324**, 153 (2004).

[55] I. Gryczynski, J. Malicka, J. R. Lakowicz, E. M. Goldys, N. Calander, and Z. Gryczynski, Thin Solid Films **491**, 173 (2005).

[56] F. D. Stefani, K. Vasilev, N. Bocchio, F. Gaul, A. Pomozzi, and M. Kreiter, New J. Phys. **9**, 21 (2007).

[57] E. Le Moal, E. Fort, S. Lévêque-Fort, F. Cordelières, M.-P. Fontaine-Aupart, and C. Ricolleau, Biophys. J. **92**, 2150 (2007).

[58] M. Trnavsky, J. Enderlein, T. Ruckstuhl, C. McDonagh, and B. D. MacCraith, J. Biomed. Opt. **13**, 054021 (2008).

[59] K. Ray, M. H. Chowdhury, and J. R. Lakowicz, Chem. Phys. Lett. **465**, 92 (2008).

[60] N. Karedla, A. I. Chizhik, I. Gregor, A. M. Chizhik, O. Schulz, and J. Enderlein, ChemPhysChem **15**, 705 (2014).

[61] R. Badugu, H. Szmacinski, K. Ray, E. Descrovi, S. Ricciardi, D. Zhang, J. Chen, Y. Huo, and J. R. Lakowicz, ACS Photonics **2**, 810 (2015).

[62] S. Z. Uddin, M. R. Tanvir, and M. A. Talukder, J. Appl. Phys. **119**, 204701 (2016).

[63] K. J. Vahala, Nature (London) **424**, 839 (2003).

[64] X. Wang, W. Ma, J. Zhang, G. Salamo, M. Xiao, and C. Shih, Nano Lett. **5**, 1873 (2005).

[65] A. I. Chizhik, A. M. Chizhik, D. Khoptyar, S. Bär, A. J. Meixner, and J. Enderlein, Nano Lett. **11**, 1700 (2011).

[66] Y. Dumeige, R. Alléaume, P. Grangier, F. Treussart, and J.-F. Roch, New J. Phys. **13**, 025015 (2011).

[67] Q. Xu, C. Piermarocchi, Y. V. Pershin, G. Salamo, M. Xiao, X. Wang, and C.-K. Shih, Sci. Rep. **4**, 3953 (2014).

[68] A. Konrad, M. Metzger, A. M. Kern, M. Brecht, and A. J. Meixner, Nanoscale **7**, 10204 (2015).

[69] M. Ediger and J. Forrest, Macromolecules **47**, 471 (2013).

[70] K. Paeng, H.-N. Lee, S. F. Swallen, and M. Ediger, J. Chem. Phys. **134**, 024901 (2011).

[71] K. Paeng and M. Ediger, Macromolecules **44**, 7034 (2011).

[72] K. Paeng, S. F. Swallen, and M. Ediger, J. Am. Chem. Soc. **133**, 8444 (2011).

[73] T. Plakhotnik, Curr. Opin. Solid State Mater. Sci. **21**, 25 (2017).

[74] G. Davies and M. Hamer, Proc. R. Soc. A **348**, 285 (1976).

[75] L. Novotny and B. Hecht, *Principles of Nano-Optics* (Cambridge University Press, Cambridge, 2012).

[76] N. Karedla, S. C. Stein, D. Hähnel, I. Gregor, A. Chizhik, and J. Enderlein, Phys. Rev. Lett. **115**, 173002 (2015).

[77] C. Lethiec, F. Pisanello, L. Carbone, A. Bramati, L. Coolen, and A. Maitre, New J. Phys. **16**, 093014 (2014).

[78] M. Born and E. Wolf, *Principles of Optics: Electromagnetic Theory of Propagation, Interference and Diffraction of Light* (Elsevier, Oxford, 2013).

[79] B. Richards and E. Wolf, Proc. R. Soc. A **253**, 358 (1959).

[80] D. Khoptyar, R. Gutbrod, A. Chizhik, J. Enderlein, F. Schleifenbaum, M. Steiner, and A. J. Meixner, Opt. Express **16**, 9907 (2008).

[81] J. Enderlein, Chem. Phys. **247**, 1 (1999).

[82] Q. Zhan, Adv. Opt. Photonics **1**, 1 (2009).

[83] T. Ruckstuhl and D. Verdes, Opt. Express **12**, 4246 (2004).

[84] M. A. Lieb, J. M. Zavislan, and L. Novotny, J. Opt. Soc. Am. B **21**, 1210 (2004).

[85] S. M. Dutra and P. L. Knight, Phys. Rev. A **53**, 3587 (1996).